

Tor Vergata University

Department of Computer Engineering

Date: March 10, 2019

I HEREBY RECOMMEND THAT THE THESIS PREPARED UNDER MY
SUPERVISION BY

Prof. Ernestina Cianca

ENTITLED

**Measuring the Water-Flow Velocities of rivers by Synthetic
Aperture Radar**

BE ACCEPTED IN PARTIAL FULFILLMENT OF THE REQUIREMENTS FOR
THE DEGREE OF

MASTER IN SPACE ENGINEERING

Thesis Advisor
Prof. Ernestina Cianca

Thesis Reader Dr. Filippo
Biondi

Chairman of Department
Prof. Ernestina Cianca

Measuring the Water-Flow Velocities of rivers by Synthetic Aperture Radar

By

Dr. Filippo Biondi

Dissertation

Submitted in Partial Fulfillment of the Requirements
for the Degree of Doctor of Master
in Computer Engineering
in the School of Engineering at
University of Tor Vergata, 2019

Rome, Italy

Scripta Volant Verba Manent (Ennio De Giorgi)

This Thesis is Dedicated to My Mother, my Father and to my Family Stefania, Manuel and Amy who decided to walk this "space adventure" together with me.

Acknowledgments

I would like to thanks all the people of the Joint Satellite Remote Sensing Center (CITS), in particular, the Research and Development Office (PSAI). I also Thank Colonel Attilio Vagliani for the work he has dedicated to CITS. He transformed a military satellite center, having standard and routinely duties only, into a Space Center of Excellence where, when he left, the processing of satellite data was covering a crucial role. This part of the space work-flow is a primary concerning task for transforming Italy into a World space power. I would like to thanks also Luca Brocca, Angelica Tarpanelli and Tommaso Moramarco of the "Istituto di Ricerca per la Protezione Idrogeologica" (IRPI) Perugia (Itlay), for providing me support and all the measurements useful for performing the experiments.

Dr. Filippo Biondi

Department of Computer Engineering
Tor Vergata University Rome (ITALY)
2019

ABSTRACT

The objective of this manuscript is to perform precise measurement of rivers velocities using synthetic aperture radar (SAR). Today a worldwide database containing the historical and reliable data concerning the water surface speed of rivers is non-existent. This research has the objective for contributing to solving this problem designing SAR processing techniques which are able to perform water flow velocity estimation. The problem of measuring such velocity is solved designing the along-track interferometry (ATI) SAR geometry which is constituted of using two radars spatially distanced by a baseline extended in the azimuth direction. In the case of space-borne missions, it is unusual to perform ATI because the designation of real-time SAR observations spatially distanced by an along-track physical baseline is a difficult task. For several monocular space-borne SAR satellite systems, the refocusing of ATI observations from one raw data can be a problem because of the under-sampled nature of the received electromagnetic bursts. This phenomenon is practiced for onboard memory space saving which makes data appearing like a white random process, making interlaced Doppler bands completely disjoint. This phenomenon, after the range-Doppler focusing process, causes decorrelation when considering the ATI interferometric phase information retransmitted by distributed targets. Space-borne line of sight (LOS) velocity measurements could be taken into consideration only for small and very coherent targets and in any case located within the same radar resolution cell. This manuscript is proposing the application of two techniques for measuring the surface water velocities of rivers. The first method

uses the multi-chromatic analysis (MCA) which is applied in the Doppler domain and combined to along-track SAR interferometry (MCA-ATI-SAR) is used to measure the range velocity component of water. For developing this technique some airborne full polarimetric SAR data observed by the uninhabited aerial vehicle synthetic aperture radar (UAVSAR) has been processed. For developing the second technique, which is based on the magnitude analysis only where several COSMO-SkyMed data-set has been used. This research was found to be suitable for finding excellent solutions for the experimental results thanks also to the high level of information which is embedded in the single SAR raw product.

Table of Contents

1	Introduction	1
2	Along-track interferometry introduction	3
2.1	Pixel-tracking introduction	5
2.2	Using radars for rivers velocity estimation	7
3	Experiment case number one methodology (multi-chromatic analysis along-track interferometry synthetic aperture radar (MCA-ATI-SAR))	12
3.1	Doppler sub-apertures formation	15
4	Experiment case number two methodology (Pixel Tracking for River Velocity Estimation)	18
4.1	Experiment case number one Experimental Results	19
4.1.1	Experiment case number one - Processing Scheme	19
4.1.2	Experiment case number one - case of study number one experimental results	20
4.2	Experiment case number one - case of study number two experimental results	21
4.3	Experiment case number one - case of study for validation	22
5	Experiment case number two Results	26
5.1	Experiment case number two - Processing Architecture and Experimental Results	28
5.2	Processing Schemes	28
5.3	Experiment case number two - case of study number one experimental results	29
5.4	Experiment case number two - case of study number two experimental results	30

5.5 Experiment case number two - case of study number three experimental results	31
6 Conclusions	33

List of Figures

6.1	Experiment case number one - computational scheme.	42
6.2	(a): Stripmap-like SAR acquisition geometry. (b): Time-frequency designation of the azimuth matched filter.	43
6.3	Multi-chromatic analysis frequency allocation strategy.	44
6.4	(a): Frequency allocation plane. (b): Spectrum of the SAR raw data. . .	44
6.5	Experiment case number one - case study one full-polarimetric SAR result.	45
6.6	Experiment case number one - case study two full-polarimetric SAR result.	45
6.7	S11 polarimetric channel SLC SAR of the study-case number one river. .	46
6.8	S11 polarimetric channel SLC SAR of the study-case number two river. .	46
6.9	S11 polarimetric channel SLC SAR of the study-case number two river. .	46
6.10	Line one river velocity profile of the study-case number two.	47
6.11	Full-polarimetric SLC data representation for data validation.	47
6.12	(a): magnitude intra-chromatic coherence. (b): phase of the intra-chromatic coherence.	48
6.13	ATI results. (a): large-swath velocity map. (b): detailed velocity map. .	48
6.14	Line one river velocity profile of the validation case study.	48
6.15	Line one river velocity profile of the validation case study.	49
6.16	Line one river velocity profile of the validation case study.	49
6.17	Line one river velocity profile of the validation case study.	49
6.18	Geometry of the rivers water-level estimation system concerning the experiment case number two. (a): Schematic representation in the range-azimuth representation plane. (b): Geometric scheme in the range-height reference plane.	50
6.19	Computational scheme concerning the experiment case number two. (a): General representation. (b): Detailed representation of the computational block number 5 concerning the range-shifts to water velocities conversion.	50
6.20	Experiment case number two - case of study number one location.	51

6.21	Experiment case number two - case of study number one footprints.	51
6.22	Experiment case number two - case of study number one ROI.	52
6.23	Experiment case number two - case of study number one SLC representation.	52
6.24	Experiment case number two - case of study number one. (a): South-East view. (b): South-East view.	53
6.25	Experiment case number two - case of study number one sub-ROI representation.	53
6.26	River water-levels heights. (red): Estimated by CSK. (blue): ground-truths.	54
6.27	River water-levels heights errors. (blue): measurement errors existing between the CSK observations versus ground-truths (no average). (red): Measurement errors existing between the CSK observations versus ground-truths (average window of 5 observations). (black): Measurement errors existing between the CSK observations versus ground-truths (average window of 10 observations).	55
6.28	Experiment case number two - case of study number two SAR footprints.	56
6.29	Experiment case number two - case of study number two ROI.	56
6.30	Experiment case number two - case of study number two SLC representation.	57
6.31	Experiment case number two - case of study number two. (a): South-East view. (b): South-East view.	57
6.32	Experiment case number two - case of study number two sub-ROI representation.	58
6.33	River water-levels heights. (red): Estimated by CSK. (blue): ground-truths.	59
6.34	River water-levels heights errors. (blue): measurement errors existing between the CSK observations versus ground-truths (no average). (red): Measurement errors existing between the CSK observations versus ground-truths (average window of 5 observations). (black): Measurement errors existing between the CSK observations versus ground-truths (average window of 10 observations).	60
6.35	Geocoded SAR images.	61
6.36	(a): Marconi bridge located in Rome. (b): Estimated velocities.	62

List of Tables

4.1	Table 1. UAVSAR Data Full-Polarimetric Additional Details	25
4.2	Table 1. UAVSAR Data versus station measurements	25

CHAPTER 1

Introduction

The author is proposing two signal processing (SP) methods for exploiting river velocities which are tailored on two different sensors. The first technique uses the multi-chromatic analysis (MCA) implementing the along-track interferometry (ATI) SAR. This new investigation technique has been called MCA-ATI-SAR. All the experimental results using MCA-ATI-SAR are estimated processing stacks of uninhabited aerial vehicle (UAV) synthetic aperture radar (SAR), (UAVSAR) data and referring to the experiment case number one. The second SP method, populating the results constituting the experiment case number two, used the investigation of the magnitude only, recorded into the single-look complex (SLC) of several long temporal series of interferometric SAR images. This information has been used for estimating the river heights with respect to some fixed reference points like some bridges. The time-variant pixel position estimation of this scattering phenomena is equivalent to estimating the river heights. Tracking the double-bounce scattering through time gives information about the distance existing between the bridge and the river surface. This space-time gap permits the indirectly retrieving of the river velocity knowing the physical model of its containment basin. The author implemented a pixel-tracking algorithm which was found extremely efficient in following the double-bounce scattering events plots, which changes its range position during time due to the river water surface level variation. This SP technique is tailored to the investigation of the COSMO-SkyMed (CSK) satellite data. The UAVSAR data was observing rivers of the United States of America (USA) terri-

tory, recasting in the experiment case number one and for the experiment case number two, the CSK satellite was observing the Italian territory. This research describes the two implemented SP methods having different nature and both designed for the same task which is the estimation of rivers surface water-flow velocities. The author imposed on both methods the constraint of processing only one SAR image which was found to be a sufficient statistic. This introduction section will be split into paragraph 2, devoted to recalling research works concerning the ATI SP, paragraph 2.1 designed to recalling some research works related to pixel-tracking and the last paragraph giving information about the use different types of radars in performing remote sensing activities with the objective to observe some principal river parameters (paragraph 2.2).

CHAPTER 2

Along-track interferometry introduction

Along-track interferometry (ATI) is a SAR investigation technique which uses the combination of two or more SAR images observing the same scene. The geometry of the SAR acquisition is constituted of two radars spatially distanced by a physical baseline extended in the azimuth direction (along-track) and parallel to the flight path. According to the ATI-SAR remote sensing configuration, images are observing targets within a short time interval. This dual-radar geometry using the along-track temporal baseline separation strategy, allows a phase difference estimation from all coregistered pixels which are proportional to the Doppler shifts of the backscattered signals. The ATI geometric SAR configuration was firstly proposed in [1] and [2] where authors described a new method for measuring the surface sea currents. The experimental results used several sets of satellite and airborne data of SAR observations. The global monitoring of river discharges can recast into a technologically challenging problem, with important applications in a variety of disciplines. Due to the limited availability and/or quality of river runoff data from many regions, an increasingly using of remote sensing techniques is highly desirable because of the vast area coverage of rivers around the world. The ATI-SAR capabilities of state-of-the-art imaging radars on satellites will also permit the high-resolution line-of-sight surface current measurements. In [3] and [6] authors presented one of the first studies concerning the ocean current estimation using ATI. Data were acquired by the shuttle radar topography mission (SRTM) where the

geometry resulted effective adding an auxiliary antenna parallel to the azimuth track and having 7m of spatial separation. Authors of [7] successfully performed airborne ATI SAR observations over the Rhone river in France. Results of the specific sensor called RAMSES gave the precise LOS velocity estimation of surface water rivers under test. The main recursive problem of ATI observations is that Doppler frequency of the radar backscatter from the ocean is not exclusively determined by the mean surface current, but it includes contributions associated with the surface wave motion. Research [4] presented an efficient new model for the simulation of Doppler spectra and ATI signatures. The model was based on the Bragg scattering theory in a composite surface model approach. Theoretical possibilities and limitations due to this problem was studied and the authors found that best results can be expected from ATI systems operated at high microwave frequencies like 10 GHz (X band), high incidence angles like 60, low platform altitude/speed ratios, and vertical (VV) polarization. Research [5] presented the first analysis of surface current fields derived from TerraSAR-X ATI data. The images were acquired over the mouth of the Elbe river (Germany) during six satellite overpasses in spring and summer 2008, using the experimental âaperture switchingâ mode of TerraSAR-X. The ATI performance of TerraSAR-X was found to be basically consistent with theoretical expectations estimating water currents variating between the range from ± 0.11 to ± 0.08 m/s in five of the six cases with one outlier at $+0.42$ m/s. In [8] authors used L- and C-band ATI-SAR measurements acquired at the Ulsan coast in the southeastern part of the Korean peninsula in order to retrieve the ocean surface current vectors. Results were compared with in-situ measurements collected by recording current meter. Authors of [9] proposed three classes of estimators which exploited multi-baseline ATI acquisition and Doppler resolution for robust data inversion under different degrees of a priori information about the wind direction and the value of the characteristic Bragg frequency. Performance analysis and comparison

with conventional ATI show that the proposed estimators can produce accurate velocity estimates in the absence of detailed ancillary data. In [10] the author summarized an analysis of gradient-induced distortions in the surface current estimates generated by ATI-SAR systems using an airborne sensor compounded in a dual-beam ATI-SAR system designed to estimate the surface current vector using only a single aircraft pass. Authors of [11] employed a pair of interferometer beams, one squinted forward and one squinted aft. Results observed the azimuthal displacement of interferometric phases by moving surfaces identical to those of conventional SAR and found that such displacement could bias the estimated surface velocity. Authors of [12] performed simultaneous measurement of terrain heights and currents using an airborne interferometric SAR (InSAR). For the first time, a hybrid two-antenna INSAR system with both along- and across-track baseline components are used to measure high-resolution digital elevation maps (DEMs) and current fields in a Wadden sea area. This research demonstrated the feasibility to perform ATI synthesizing two ATI observations by Doppler sub-apertures.

2.1 Pixel-tracking introduction

Tracking activity is largely used in SAR, this SP procedure allows the precise space offset measurement of pixels located on coregistered images, composing a long temporal series of SAR data, observing the same scene with the same geometry. This research implemented a tracking technique based on localized spectral analysis, with the objective to estimate the river water-flow velocities. As mentioned in the previous section, this task is normally performed using the pure-Academic ATI technique. The problem of refocusing MCA-ATI observations from a single raw data using CSK is generated from the not over-sampled nature of the received electromagnetic bursts. This phenomenon is practiced with the objective to perform onboard memory space compression which

makes data very similar to a white random process. This characteristic makes appearing interlaced Doppler bands completely disjoint and after the range-Doppler focusing process, causes decorrelation when considering the single-pass ATI interferometric phase information retransmitted by distributed targets. This research is proposing the application of a more robust technique designed to track in time the double-bounce reflections of some coherent scatterers like some bridges crossing the rivers. This technique measures the gap in space existing between the river surface and bridges which are observed perpendicular to the slant-range direction. This space-gap existing between the single-bounce backscattered echoes generated by the principal structures of the bridge and the double-bounce scattering events reflected on the river surface, which can be observed into the SLC SAR image, is tracked in time. This space-gap is proportional to the time-domain water displacement. River water-flow data are indirectly retrieved by converting the time-domain water surface displacement variation into water-flow velocities. The experiments are evaluated processing long temporal series of CSK data. Several methods were used during the past to remotely sensing the surface water velocity of rivers. In [33] the rivers surface currents have been measured using coherent microwave systems. In [18] authors developed a new algorithm that automates the calculation of river widths using raster-based classifications of inundation extent derived from remotely sensed imagery. In [19] an infrared-based measurement of Velocity system considering the turbulent kinetic energy, and dissipation at the water surface in a tidal river has been developed. In [20] the capability of coupling measurements of river velocity derived from Moderate Resolution Imaging Spectroradiometer (MODIS) and water levels derived from ENVISAT Advanced Radar Altimeter (RA-2) for river discharge estimation was successfully investigated. In [21] authors performed the first step toward in situ natural flow measurements with a new biologically inspired probe design in conjunction with signal processing methods. Several works have been made in the field of

pixel tracking where image alignment is a crucial step for interferometric SAR (InSAR). Interferogram formation requires images to be coregistered with an accuracy of better than a few tenths of a resolution cell to avoid significant loss of phase coherence. For InSAR products coregistration a 2-D polynomial of low degree is usually chosen as warp function, and the polynomial parameters are estimated through least squares fit from the shifts measured on image windows [17]. Some tracking technique has previously been applied to monitor glacier movements, volcanic activities and co-seismic tears in the solid earth resulting from severe earthquakes to address the technical defects and limitations of conventional differential InSAR (DInSAR) techniques, particularly their sparse coverage and the impact of dense vegetative cover [14]. In the past, studies on offset tracking techniques to measure slope movements were dominated by using optically sensed imagery from spaceborne or airborne platforms. For low-resolution SAR sensors, offset tracking is used for measuring very large deformation [13]-[14]-[15]-[16].

2.2 Using radars for rivers velocity estimation

The work presented in [23] exploited the long and single TerraSAR-X Staring Spotlight (ST) SAR acquisition to derive the absolute heights of targets. The topic exploited the slight azimuth defocusing effect due to height mismatch between the true height and the height assumed in SAR focusing as a resource. This technique could be used to retrieve absolute heights with accuracy depending on incidence angle, orbit type, and mainly on the signal-to-clutter ratio. Research [24] performed the characterization of the floodplain processes and discussed the reaction of a large model river to a hill-slope supply of eroded masses using a mass balance data from Asian rivers together with a first-order diffusive simplification of the St. Venant-Exner equations. The work showed the system converging towards a state in which reacted to perturbations in the erosion of the land-

scape by small-amplitude oscillations around an average balanced on a stationary state. A rigorous velocity equation designation for open channel flow was derived in [26]. The equations described the application of a probabilistic formulation solving the problem of the river water-flow velocity distribution estimation. According to the basic hydrodynamics laws characterizing the water flowing through an open channel cross-section, efficient modeling and simulation of the velocity distribution of the water surface, flowing through an open-channel, has been also developed. Conventional measurements of river flows are costly, time-consuming, and frequently dangerous. The work performed in [25] reports the evaluation of using a remote sensing solution constituted by a continuous wave radar, a monostatic UHF Doppler radar, a pulsed Doppler microwave radar, and a ground-penetrating radar to measure river flows continuously over long periods and without touching the water with any other instrument. The experiments successfully duplicated the flow records from the conventional stream gauging stations on the San Joaquin River in California and the Cowlitz River in Washington. In [27] the phase speeds of both upwind and downwind traveling, wind-generated water waves 4.1, 9.8, 16.5, and 36 cm in wavelength were successfully measured by using microwave Doppler spectrometry. Microwave signals backscattered from the oceans and lakes have been collected at many different wind speeds and fetches. Doppler spectra of some signals obtained at low microwave frequencies exhibit double peaks clearly indicating Bragg scattering. Research also found that at higher microwave frequencies, high wind speeds, long fetches, or in the presence of substantial swell, these splittings disappeared. A model of microwave Doppler spectra based on Bragg-scattering, composite-surface theory has been developed and used to show that the results obtained in these field studies were compatible with the hypothesis that Bragg scattering dominates microwave backscatter from rough water surfaces under many wind speed and incidence angle conditions [28]. Authors of [29] performed coherent microwave backscatter measurements at

the Ku electromagnetic band observed from the gondola of the airship and micrometeorological and wave height measurements made from an airborne platform suspended by a cable 65 m long located below the gondola in order to be set between 5 and 20 m above the sea surface. Results gave very precise measurements of the water-flow velocities. River surface currents have been measured using coherent microwave systems installed on bridges, cableway, riverbanks, helicopters or airplanes. In most cases, the microwave measurements have been compared with conventional measurements of the near-surface currents and found to be accurate to within about 10 cm/s. In all cases, the basis for the microwave measurements of the surface currents is the Doppler shift induced in the signal backscattered from the rough water surface. In research [30] a time series of surface velocity and stage have been collected simultaneously. Surface velocity was measured using an array of continuous-wave microwave sensors. Results clearly showed the feasibility to measure water velocity using the estimation of the electromagnetic Doppler effect. According to [31] a coherent X-band airborne radar has been developed to measure wind speed and direction simultaneously with directional wave spectra on the ocean. The coherent real aperture radar (CORAR) measured the received power, mean Doppler shifts, and mean Doppler bandwidths from small-resolution cells on the ocean surface and converts them into measurements of winds and waves. In [32] the authors used continuous-wave (CW) microwave systems which have been anchored over a bridge in order to ensure long-term measurements of the surface currents. The results were compared with current-meter measurements and with some time series observed by different sensors stage. The research described how compact CW system has been developed and used on a cableway in measuring surface currents at various distances across a river. The collected measurements have been compared with other alternative acoustic data observing the same scene. The same research showed how pulsed Doppler radars have been used to measure river surface currents from a riverbank. The sensor

was installed on-board a helicopter and an airplane. The research showed also that the CW system was preferable to use instead of using pulsed Doppler radars to make such measurements from helicopters. Finally, [33] considered the implications for measuring the surface currents from aircraft or satellites using INSARs geometries, finding that a combination of along-track and cross-track INSAR is necessary but those significant limitations are inherent in the technique. Research [34] considered a two-scale model of rough surfaces is considered which permitted the theoretical interpretation of the features of very high-frequency scattering from the sea surface). The experimental measurements were carried out using wavelengths set to 3.2 cm, 10 cm, 50 cm, 1.5 m, and 4 m and observing shifts of the central frequency agreeing with the results of other authors (for the range of $a=3$ cm to 200 m). Space correlation of the backscattered signal was also investigated (both theoretically and experimentally) finding 50% of decorrelation occurring at all distances compared with the average dimensions of the wave slope. Research [35] considered the scattering effects from very high frequency (VHF) radar pulses from a random weakly corrugated surface using a perturbation investigation method. Results showed that the spectrum of the scattered radiation shifted respect to the incident central frequency by a certain value related to the phase velocity generated by the surface water-flow velocity. The work developed in [36] reviewed the basics of SAR theory of ocean wave imaging mechanisms, using both known work and recent experimental and theoretical results from the Marine Remote Sensing (MARSEN) Experiments. From the analysis has emerged a more complete view of the SAR imaging phenomenon that has been previously available, generalizing also a new imaging model approach. In [37] surface velocities has been measured using a pulsed Doppler radar, and river depth has been estimated using ground-penetrating radar. Surface velocities were converted to mean velocities, and horizontal registration of both velocity and depth measurements enabled the calculation of river discharge. The magnitude of the

uncertainty in velocity and depth indicated that the method error was located around a range of 5 percent. The results of the experiments indicated that the helicopter-installed radar could potentially perform a rapid and accurate radar observation predicting the exact locations of floods. Research [38] reviewed and extended the current models on the imaging mechanism of water currents. A linear transfer functions that related some two-dimensional wave fields to the real aperture radar (SLAR) image where calculated by using a newly developed two-scale wave model. It is noted that a description of the imaging process by these transfer functions can only be adequate for low to moderate sea states. Results compared the theoretical models for the imaging mechanisms with existing SLAR and SAR imagery of ocean waves and concluded that the author's theoretical models were in agreement with experimental data. In particular, the author's theory predicted that swell traveling in flight (azimuthal) direction is not detectable by SLAR but was only detectable by SAR systems. In [39] a two-frequency microwave technique at slanting incidence for the measurement of ocean wave spectra has been investigated in more detail with respect to its applicability in aircraft and space vehicles. It was shown that by carrying out an efficient signal processing in the frequency domain the system-inherent signal-to-noise ratio could be increased considerably, making the operation of the system from air- and space-borne platforms feasible. The remainder of this manuscript is organized as follows. In section 3, a detailed description of the ideas behind the proposed procedure is provided, whereas in Sections 4 and 3.1 the theoretical model for the SAR and definition of the MCA and sub-apertures architecture are presented. Section 4.1 is devoted to the MCA-ATI-SAR SP technique. Section 5 is totally dedicated to exploring some practical examples and experimental results based on estimating river velocities exploiting the magnitude tracking algorithms and processing CSK data. The computational architectures are described in sections 5.1 and 5.2. Finally, some concluding remarks and future research tracks are given in Section 6.

CHAPTER 3

Experiment case number one methodology (multi-chromatic analysis along-track interferometry synthetic aperture radar (MCA-ATI-SAR))

The ATI technique is based on the interferometric combination of two SLC SAR images observing the same scene. The images must be formed between a short time interval varying from some milliseconds to a few seconds. The phase differences between all range-azimuth resolution cells composing the two images are proportional to the Doppler shifts of the backscattered signals. To obtain two ATI-SAR images with a short time delay from a moving platform, it is necessary to install on-board two antennas separated by the corresponding spatial baseline oriented along the flight direction. Accordingly, the technique is called ATI, which is different if compared to the cross-track interferometry (XTI) where the spatial baseline is 90° tilted and used for topographic reconstruction. ATI considers conventional SAR observations augmented with two sensors having a spatial baseline parallel to the radar velocity (along-track slow-time dimensionality) vector component. The backscattered SAR echoes received from each antenna are processed separately forming two independent images and having different Doppler history. The LOS velocity of targets is estimated by interference and the information is evaluable pixel by pixel according to the following phase difference which is proportional to the

ATI spatial baseline:

$$\phi = \frac{4\pi uB}{\lambda v}. \quad (3.1)$$

In (3.1) λ is the electromagnetic wavelength, B is the along-track spatial baseline, v is the radar velocity and u is the LOS speed component of the targets. This research considers the estimation of the river water-flow velocity by ATI using only one SAR image. The used technique was the application of the Doppler sub-apertures SP which are used to synthesized a couple of SAR images having a spatial distance between the master and the slave. The technique permits azimuth refocusing at different Doppler sub-bands, accepting a cross-range resolution loss. The azimuth resolution loss could be quantified approximately the 45% with respect to the total Doppler band amount. The author defines this new SP approach a technique called MCA-ATI-SAR. The basic principle is the diversification of along-track views assumed from the radar anchored on a flying platform during a single SAR acquisition [23]. In this article, the validation of the technique is defined by processing several observations of SAR data-sets collected by the NASA-UAVSAR airborne sensor. The method proposed in this research requires only a single SAR acquisition in order to emulate a dual-sensor ATI-SAR geometry, this proposed technique is more convenient respect to the classical because using only one image. The experimental results are focused to estimate the river water-flow velocities. Fig. 6.2 represents the frequency allocation plane constituted by refocusing the raw SAR image using two different sub-apertures. Both sub-products have less resolution with respect to the original unique full-band product. In order to perform all the experiments, the author has produced two sub-products where the reducing in azimuth resolution of the 45% with respect to the total Doppler Band was fount an optimum value. The two

refocused sub-bands are not overlapped, this band allocation strategy is compatible with the frequency allocation scheme. In this configuration, the sub-apertures are refocused on a large along-track baseline which is an optimum condition for observing low velocities with high sensitivity. According to Fig. 6.2 the author gave for the first Doppler sub-aperture the values starting from 0 Hz to 2.75 kHz and for the second sub-aperture assigning all the frequencies starting from 2.25 kHz to 5 kHz which represents the maximum available Doppler frequency. For this specific airborne case, has been performing ATI and achieving excellent results using only one raw image. This strategy was found to be the best choice because data is not under-sampled. In the case of spaceborne missions is very difficult to perform ATI starting from a large-band single-antenna image because at least two real-time SAR observations spatially distanced by a baseline are needed. For spotlight spaceborne SAR re-synthesizing two ATI observations from one raw data is a problem because the received electromagnetic bursts are not oversampled for onboard memory space saving and data appears like a white random process. This problem makes appearing interlaced Doppler bands completely disjoint. This phenomenon, after the range-Doppler focusing process, causes severe decorrelation when considering the ATI interferometric phase information retransmitted by distributed targets. It could be taken into consideration only small and very coherent targets and in any case located within the same radar resolution cell. This is not the case of the UAVSAR data which seems to have a sufficient level of oversampling factor. Fig. 6.4 (a), (b) represents the spectrum of the UAVSAR raw of one range line (Fig. 6.4 (a) which is depicted with the red line) and one azimuth line (Fig. 6.4 (b) plotted by the red line) which is compared to a simulated white random process which is typically associated to the raw data observed by a SAR satellite system. The random processes are collected along a range and an azimuth line which is depicted in the same order in Fig. 6.4 (a) and (b) but in the blue line. The random process spectrum remains constant along all

the frequencies but the spectrum of the UAVSAR data is not constant because energy accumulation areas can be visible on the edges of the spectrum. This phenomenon is a symptom of a well-sampled signal and therefore it is rich in information particularly indicated for this single-image Doppler analysis.

3.1 Doppler sub-apertures formation

The basic idea of MCA is to split into two or multiple sub-apertures D_i the overall Doppler bandwidth D generated by the transmitted SAR electromagnetic impulse during the azimuth SAR image formation. According to Fig. 6.3, which is a general multiple case, the Doppler band is split into N sub-apertures having each central frequency centered at f_i with $i = 1 \dots N$ and $f_1 > f_2 > \dots > f_N$. The result of the MCA analysis is the generation of a stack of range-azimuth SLC SAR data, focused according to an ascending stepped central Doppler frequency strategy. Each sub-aperture is characterized to have minor band occupancy if compared to the original full-band Doppler burst collections. A radar designed for Earth observation use, performs azimuth focusing due to the deterministic source coding having the same principles of the chirp signal generated in range and due to the velocity of the platform. The azimuth resolution is directly proportional to the total Doppler band. Each back-scattered slow-time records contains all the frequencies between the azimuth bandwidth limits. Considering the radar geometry depicted in Fig. 6.2 (a), constituted of one active SAR sensor positioned to a certain height, moving with a velocity v parallel to the azimuth direction and the radar is illuminating the ground, transmitting electromagnetic pulses LFM centered at f_0 with a certain azimuth aperture. In Fig. 6.2 (a) are visible three point targets. Target 1 retransmitting the radar echoes tuned to a higher frequency, with respect to the carrier frequency f_0 and equal to $f_0 + f_D$ where the parameter f_D is the Doppler frequency

shift equal to:

$$f_D = \frac{2v_r}{d_{LOS}}. \quad (3.2)$$

In (3.2) the parameter v_r is the platform velocity and d_{LOS} is the radar-target LOS distance. According to Fig. 6.2 (a), The zero-Doppler line is approaching Target 2 when the azimuth reference system is orthogonal to the parameter d_{LOS} . The backscattered echoes of Target 3 has less frequency because the parameter d_{LOS} is increasing away from the platform. All the azimuth echoes located in each line has to be compressed using the matched filter where this is performed on the ground in post-processing. The azimuth resolution is equal to the following equation:

$$\delta_a = \frac{\lambda R_{LOS}}{2d}. \quad (3.3)$$

Equation (3.3) is only valid for the stripmap-like SAR acquisitions and the parameters λ and d are the wavelength and the azimuthal footprint length respectively. Considering an environment constituted only by one point target, the recorded azimuthal function can be expressed, in the time domain, by the following convolution:

$$r(t) = s(t) \star c(t). \quad (3.4)$$

In (3.4) the function $s(t)$ is a point target distribution function and $c(t)$ is the received electromagnetic azimuthal history. Due to Doppler, this function is LFM, according to

the modulation scheme depicted in Fig. 3.4 (b). In order to extract the ground information, the received signal, has to be compressed designing an adapted filter, matched to the azimuthal Doppler history, according to the slow-time versus frequency scheme showed in Fig. 3.4 (c). Such a system has to be dimensioned having a descending chirp rate, opposite to the received Doppler history having a certain linear frequency variation rate, set at $\mu = 2\pi \frac{D}{T}$. The compressed signal, the one spilled from the compressor output, can be expressed as:

$$r_c(t) = s(t) \star c(t) \star c'(t) \text{ where } c'(t) = c^\dagger(-t) \text{ and} \quad (3.5)$$

$$F[r_c(t)] = S(f)|C(f)|^2.$$

The SAR response of a point scatterer, in the range direction is so:

$$r_c(t) = D \operatorname{sinc}(\pi D(t - 2R/c)) \cdot \exp(J2\pi f_0 t) \cdot \exp\left(\frac{4\pi R}{\lambda}\right). \quad (3.6)$$

Where, after a base-band down-conversion procedure, the recorded signal is:

$$r_c(t) = D \operatorname{sinc}(\pi D(t - 2R/c)) \cdot \exp\left(\frac{4\pi R}{c/f_i}\right), i = 1 \dots N. \quad (3.7)$$

In order to proceed in exploiting the experimental results the author implemented the model (3.7) using only two non-overlapped bands.

CHAPTER 4

Experiment case number two methodology (Pixel Tracking for River Velocity Estimation)

The problem of motion detection of targets is solved using ATI which is observed using two radars spatially distanced by a baseline extended in the azimuth direction. In the case of spaceborne missions is very difficult to perform ATI observing distributed targets because at least two real-time SAR observations spatially distanced by a baseline are needed. For spotlight spaceborne SAR re-synthesizing two ATI observations from one raw data could be a problem because of the not oversampling nature of the received electromagnetic bursts. This procedure is performed to realize onboard satellite memory space saving and in most of the cases data appears like a white random process. This problem makes interlaced Doppler bands appearing completely disjoint. This phenomenon, after performing the range-Doppler focusing process, produces decorrelation when considering the ATI interferometric phase information retransmitted by distributed targets. It could be taken into consideration the performing of ATI only for observing small and very coherent targets and in any case located within the same radar resolution cell. This manuscript is proposing a new approach where the water velocity of rivers, occupying thousands of pixels, is estimated processing the information given by sub-pixel tracking generated by the coregistration process of several multi-temporal interferometric stacks of the CSK satellite data.

4.1 Experiment case number one Experimental Results

This section is devoted to giving a detailed description of the computational scheme concerning the experiment case number one. Fig. 6.1 shows the architecture used for estimating the results for which the MCA-ATI SP technique has been used. The processing scheme was designed building-up 14 processing blocks and a detailed description concerning the function performed by each of them is now reported.

4.1.1 Experiment case number one - Processing Scheme

This paragraph is referring to the processing scheme concerning the experiment case number one and depicted in Fig. 6.1. The processing blocks number 1, 2 and 3 are composing the raw data of each polarimetric channel of the UAVSAR dataset. Each polarimetric channel is decomposed into two sub-apertures through the computational blocks number 4 and 7 for the HH channel, blocks number 5 and 8 for the HV channel and blocks number 6 and 9 for the last VV polarimetric channel. Three interferograms are built-up through processing blocks number 10, 11 and 12 for the intra-chromatic VV, HV and HH polarimetric Doppler sub-apertures respectively. The best fit estimation for the ATI velocity is performed by the computational block number 13 where the ATI interferometric phase versus velocity conversion is performed by the last processing block number 14.

4.1.2 Experiment case number one - case of study number one experimental results

This paragraph is reporting the results concerning the experiment case number one and more specifically is referring to the case study one. The velocity of a river's water-flow depends mainly upon the slope and the roughness of its channel. A steeper slope causes higher flow velocity, but a rougher channel decreases it. The slope of a river corresponds approximately to the topographic slope of the country it traverses. Near the source of the river, frequently on hilly regions, the topographic slope is usually very steep and going far away it gradually flattens out. In most of the cases digital elevation models (DEM)s are presented with occasional irregularities, until, in traversing plains along the latter part of the river's course, it usually becomes quite mild. Accordingly, large streams usually begin like torrents characterized to have highly turbulent flows as gently flowing rivers Authors of [24] used the mass balance data from Asian rivers together with a first-order diffusive simplification of the St. Venant-Exner equations to characterize river floodplain processes and discuss the reaction of a large model-river to a hillslope supply of eroded masses. The simple analytical solution derived for the long-term profile of the river bed shows that the system converges towards a state in which it reacts to perturbations in the erosion of the landscape by small-amplitude oscillations around an average stationary state. However, the results are based on three study cases where several regions of interests (ROIs) consists of a series of SAR patches representing some rivers which are observed by the UAVSAR. Explaining the context more specifically, the experimental results will be divided into two main study cases and a third experiment is dedicated to the validation of the technique where details are described in the next section. The study case number one is constituted by the following UAVSAR data: ColFor_30402_14039_010_140414090_01. The SAR image is depicted in Fig. 6.5 where the point $P1$ represents the image scene location center

which is geolocated on the following coordinates: 1.580775°N 78.618778°W. The ROI is located inside the yellow box number one depicted in Fig. 6.4. The case of study number two is constituted by the UAVSAR data having the following identification number: gulfco_05003_15057_007_150508090_01. The SAR image is depicted in Fig. 6.6 where the point $P1$ represents the image scene location center which is geolocated on the following coordinates: 29.477644°N 91.378587°W. For this study case, two ROIs are considered and located inside two yellow boxes which are visible in Fig. 6.6 and tagged by green numbers 1 and 2. Fig. 6.7 (a) is the study-case number one result where the river is correctly detected through an infra-chromatic coherence greater than 0.88. The target is the Rio Mataje located in the state of Colombia. This result is characterized to observe the water-flow velocities where the estimated maximum value is approximately 1.4 m/s and inside the yellow box is located a particular which is depicted in Fig. 6.7 (b). This picture represents the visualization of some detailed velocity information. The yellow arrow number 1 indicates a narrow channel of the river. The Author reports to the attention to the presence of an acceleration in correspondence of this bottleneck.

4.2 Experiment case number one - case of study number two experimental results

This paragraph is reporting the results concerning the experiment case number one and more specifically is referring to the case study two. Fig. 6.8 is the study-case number two result where the river is correctly detected through an infra-chromatic coherence greater than 0.80. The Image represents a tributary of the Atchafalaya River for which the study was carried out. This River is a 137-mile-long (220 km) which is the fifth largest river in North America. The Mississippi River floods in April and May 2011 were among the largest and most damaging recorded along the U.S. waterway in the

past century, comparable in extent to the major floods of 1927 and 1993. In April 2011, two major storm systems deposited record levels of rainfall on the Mississippi River watershed. When that additional water combined with the springtime snow-melt, the river and many of its tributaries began to swell to record levels by the beginning of May. Fig. 6.8 represents the velocity map of the environment contained inside the yellow box number one depicted in Fig. 6.6. The picture shows the great mouth of the river and it is possible to visualize the spatial evolution of the velocities of the river currents that are recomposed with those of the sea. Fig. 6.9 (a) represents the river portion located inside the yellow box number two depicted in Fig. 6.6. The velocities of the river are compliant to the physical principle which allows higher velocities located on the middle part of the river and lower velocities are detected along the edges. This phenomenon occurs because the edges of the river produce more friction, lowering the velocity of the water flow which becomes higher while the center of the river is approached. Fig. 6.10 represents the particulars of the environment located inside the yellow box number one which is depicted in Fig. 6.9 (b). The image shows detailed information about the river water-flow velocity. Two velocities lines are taken into account which is indicated with the yellow lines number one and two respectively. Fig. 6.10 (a) and Fig. 6.10 (b) represents the evolution of the instantaneous velocity of the river versus range which shows the compliance of the physical evolution of the water-flow.

4.3 Experiment case number one - case of study for validation

This paragraph is reporting the results concerning the experiment case number one and more specifically is referring to the MCA-ATI-SAR validation case study. The validation of the measurements are performed comparing the estimated water-flow velocities

to data observed by the water-level ground-measurement station having the following identification number: *USGS 15743850 DAHL C NR KOBUK AK*. Data are provided for free by the United-States National Water Information System web interface. The author is comparing a stack of UAVSAR data observing a portion of the US state of Alaska where the geolocated full-polarimetric SAR image is depicted in Fig. 6.11. The point $P1$ is geolocated at the following coordinates: Datum world geodetic system 1984 (WGS 84) European petroleum survey group (EPSG) 4230, Lat: 67.119946° N, Lon: 158.177811° W. The point $P2$ (the measurement station) is instead geolocated at the following coordinates: Datum WGS 84 EPSG 4230, Lat: 66.848357° N, Lon: 157.190757° W. Fig. 6.11 represents the computational scheme designed for implementing the river velocity estimation. According to the UAVSAR raw spectral configuration, the Doppler sub-apertures, for each polarimetric channel, are generated by the computational blocks number 4, 5 and 6, implementing the high-pass filter and computational blocks number 7, 8 and 9, implementing the low-pass filter. The UAVSAR sensor transmits electromagnetic bursts centered on a carrier tuned to 1.26 GHz occupying 80 MHz of chirp bandwidth which allows 3.5 m of range resolution and nearly 5 m of azimuth resolution, the illuminating swath of approximately 16 km in range. The central frequencies and the bandwidths of the LPFs and HPFs are selected according to the frequency allocation plane reported in Fig. 6.4 (a). The Doppler sub-apertures for each polarimetric channels are inputted to the computational stages number 13, 14 and 15 for the along-track interferograms formation. The computational stage 13 chooses the best values in terms of intra-chromatic coherence which gives data to be the best velocity estimation performed by the computational block number 14. The measurement station (the point $P2$) is located with respect to the SAR observation measurement $P1$, approximately 30 km far, so a small error on the experimental results comparison has to be accepted. The list of SAR data identification codes (ICs) and acquisition date are reported in Tab.

4.1. The proposed UAVSAR SAR stack was found to be the best matching to the open source data recorded by the measurement station. Fig. 6.13 (a) represents the image of the velocities map estimated on the first UAVSAR data reported in Tab. 4.1. The red-box reported in the picture represents a detailed image grab which is visible in Fig. 6.13 (b). The validation measurements for all the images composing the validation stack are spilled from the river portion ATI phase-map located inside the red box visible in Fig. 6.13 (b). The infra-chromatic coherency in magnitude and phase are reported in Fig. 6.12 (a) and Fig. 6.12 (b) respectively. The river is detected with very high coherence and consequently, the river is constituted by highly stable ATI phase information. Fig. 6.14 (a) represents the height of the water-flow observed by the measurement station, which is reporting the daily water height starting from the 01-09-2015 to 31-10-2015. The UAVSAR observation was performed on the 05-10-2015 which is indicated on the time span by a red arrow. The measurement on that day is approximately 4.9 feet. Fig. 6.14 (b) shows the discharge in cubic feet per seconds recorded during the same time-span of the previous picture. Fig. 6.14 (a) and Fig. 6.14 (b) are synchronized to the UAVSAR observation ID: permaf0310815147004151005L090, Fig. 6.15 (a) and Fig. 6.15 (b) are synchronized to the UAVSAR observation ID: ambler0300117097008170915L090, Fig. 6.16 (a) and Fig. 6.16 (b) are synchronized to the UAVSAR observation ID: PREM-LEG0300117067006170619, Fig. 6.17 (a) and Fig. 6.17 (b) are synchronized to the UAVSAR observation ID: ambler0300118054009180901L090. The results observed by the UAVSAR are compared to the observations recorded by the measurements station are reported in Tab. 4.2. The precision of the SAR measurements is confirmed by an increase of velocity correctly detected on the records number 2 reported in Tab. 4.1 and Tab. 4.2.

Number	IC	Date
1	permaf0310815147004151005L090	05-10-2015
2	ambler0300117097008170915L090	15-09-2017
3	PREMLEG0300117067006170619	19-06-2017
4	ambler0300118054009180901L090	01-09-2018

Table 4.1: Table 1. UAVSAR Data Full-Polarimetric Additional Details

Number	water height (m)	discharge (cubic-feet/s)	SAR (m/s)	velocity
1	4.9	35	0,7441	
2	5.7	280	1,1687	
3	4.75	20	0,6324445	
4	4.75	35	0,71415	

Table 4.2: Table 1. UAVSAR Data versus station measurements

CHAPTER 5

Experiment case number two Results

In this section, the experimental results estimated processing sets of CSK data has been reported. The author worked on three sets of stripmap SAR data observing three different locations. The results are referring to the experiment case number two and composed of three study cases. The first data-set, composing the case study number one, observed the Po river located on the north side of Italy and the measurements were validated comparing data recorded by the measurement station which is geolocated on the following geographic coordinates: datum world geodetic system 1984 (WGS 84) European petroleum survey group (EPSG): 4240, $44^{\circ} 53' 18.84''$ N $11^{\circ} 36' 28.89''$ E. The optical representation of the environment where the river velocities has been estimated is reported in Fig. 6.20. The measurements estimated by the satellite has been validated by comparing to the real observations recorded by the water-level measurement ground station. The second data-set was observing the Tiber river located in the center of Italy. The satellite observations were concentrated very near to the measurement ground-station geolocated on the following geographic coordinates: datum WGS 84, EPSG, $43^{\circ} 00' 37.11''$ N, $12^{\circ} 25' 45.15''$ E. The representation of the environment where the river velocities have been concentrated is reported in Fig. 6.22. Also, in this case, the data-set has been validated by comparing the measured data to the real observations of by the local measurement system. The last case study is composed only by satellite measurements inside the city of Rome, concentrating the measurements on the

Guglielmo Marconi bridge (the optical representation of the infrastructure is reported in Fig. 6.36 (a)). In reference to the experiment case number two the author is using a sub-pixel tracking technique for estimating the displacement existing between the pixels projection position on the SLC image backscattered from the radar echoes retransmitted by the lateral railings of the bridges under test and the double-bounce effects backscattered from the same target but reflecting the energy from the water surface which in this case is working like a mirror. The geometry of this electromagnetic measurement system is depicted in Fig. 6.18 (a), (b). The picture shows in Fig. 6.18 a river portion laying on the range-azimuth plane, where the water is flowing with a velocity direction parallel to the range, moving away from the sensor which is visible on the left side. A bridge is present in the middle of the figure and crossing the azimuth dimension. Fig. 6.18 (b) shows the range-height representation of the acquisition geometry. The sensor is visible on the top-left side of the picture, the range-height section of the bridge is visible at the center of the picture and the SLC projection plane is located at the top-right side. The Point P_{Ref} is visible on the SLC projection plane which is the focused single-bounce backscattered echo from the illuminated side of the bridge. The position of P_{Ref} is constant versus time. The positions of points P_1 , P_2 , and P_3 on the SLC projection screen, represents the double-bounce backscattered echoes of the same target. The distance of the two-way propagation system depends on the heights of the water levels L_1 , L_2 , and L_3 which are depending versus time. If a long temporal series of interferometric SAR images are available, following this procedure it is possible to track in time the water level of the river and so to obtain a measurement of the surface river velocity. Fig. 6.20 is the optical representation of the infrastructure used to test this technique which is located on the same geographical coordinated of the land-based measurements system. Fig. 6.23 shows the SLC image where the ROI is located inside the red box number 1.

5.1 Experiment case number two - Processing Architecture and Experimental Results

This section is devoted to giving a detailed description of the computational schemes concerning the case of the experiment case number two. Fig. 6.19 shows the architecture used for estimating the results constituting the study-case number one for which the MCA-ATI SP technique has been used. The computational scheme was designed over 5 processing blocks which are visible in Fig. 6.19 (a). The principal computational block involved in measuring the water-level height is the number five where a detailed description of its implementation is reported in Fig. 6.19 (b). A detailed description of each function of the computational scheme is reported.

5.2 Processing Schemes

This section is describing details of the proposed processing architecture and the resulting performance are investigated resorting to two study cases. The author worked on three sets of CSK data of the Italian observation mission CSK called *MAPITALY* procured by the Italian Space Agency (ASI). The first data-set, constituting the first study-case, is populated by 106 SAR images observed from the 03-05-2009 to the 16-08-2018. The second study-case data-set is constituted of 76 SAR images observed from the 21-03-2011 to the 22-04-2017. The first illustrative examples rely on a long temporal interferometric SAR acquisition representing the environment of the Po river located in the North side of the Italian state. The Region of Interest (RoI) of the second study case is located in the central part of Italy, near the city of Perugia, observing a portion of the Tiber river. A third study case was devoted in measuring the motion parameters of the same river when passing through the city of Rome. Fig. 6.3 shows the

foot-print of the long temporal series interferometric SAR stack observed by the CSK satellite system and concerning the case of study number one. Fig. 6.19 (a) is reporting the computational scheme used for estimating the river velocities. The computational block number 1 represents the data input which is constituted by sets of long temporal series of SAR data. The coregistration process is performed by the computational block number 2. After coregistration, the range shifts are recorded for an initial coarse estimation of the double-bounce shifts and errors correction. The ROI extraction is performed by block number four and the last computational block (the number five) performs the precise range shifts estimation and velocities conversion. Fig. 6.19 (b) shows the detailed description of the computational block number five, constituted by the computational block number 5.1, representing the data-input ROI, inputted in the computational block 5.2 representing the SAR sub-ROI extraction, concerning a detailed image patch constituted only by the bridge. Computational block number 5.3 performs the azimuth average of the sub-ROI and computational block 5.4 performed the one-dimensional fast-Fourier transform (FFT). The last computational stage (block number 5.5) converts very little shifts given by a small space variation to a mass variation. The estimation of this mass variation is compensated to the range variation shifts estimated by the coregistration stage.

5.3 Experiment case number two - case of study number one experimental results

This paragraph is reporting the results concerning the experiment case number two and more specifically is referring to the case study one. Fig. 6.21 represents the footprints of the study-case number one consisting of a long-temporal series of interferometric SAR images. The ROI is located inside the footprint and constituted by the small red box

tagged with yellow number two. The ROI is represented in detail by Fig. 6.22 where the bridge is observed by an optical image and contoured by the same red box. The recording base-station which is devoted to collect all the ground-truths data is located very near the yellow benchmark called *Pontenuovo* which is geolocated on the following coordinates: datum WGS-84 (EPSG): 4240, $44^{\circ} 53' 18.84''$ N $11^{\circ} 36' 28.89''$ E. With reference to Fig. 6.23, the small red patch number one is containing the bridge used for processing data, which is shown in details in Fig. 6.24 (a) and (b). Fig. 6.25 is the sub-ROI representation consisting of the data input of the computational block number 5 depicted in Fig. 6.19 (a) and (b). The Sub-ROI magnitude shows the bridge structure constituting collecting the backscattered radar energy and populating the range pixel line consisting of the spatial reference point and tracked by the pink layers L_1 and L_2 . The variance of the double-bounce layovered backscattered echoes is located inside the spatial gap contained by the blue layers L_3 and L_4 . The temporal trend of this layover scattering line is a function of the river water level. The trend of the estimated water levels are depicted in Fig. 6.26. The blue line represents the water-levels measured by the CSK satellite system and the red function represents the ground-truths given by the ground observation station.

5.4 Experiment case number two - case of study number two experimental results

This paragraph is devoted to showing results concerning the experimental case number two and referring to the case of study two. This new experiment shows the observation of the Tiber river captured when it crosses the territories of the Italian central Apennines located in the Umbrian region. In this context, the Tiber is narrower than the Po river studied previously and the radar observations are noisier so this case study can

be considered more difficult to explore with respect to the previous one. Fig. 6.28 represents some footprints of the study-case number one consisting in a shorter long-temporal series of interferometric SAR images. The ROI is located inside the footprint and constituted by the small red box tagged with the yellow number one. The ROI is represented in detail by Fig. 6.29 where the bridge is observed by an optical image and contoured by the same red box. The recording base-station which is devoted to giving all the ground-truths data is located very near the yellow benchmark called *Pontenuovo* which is geolocated on the following coordinates: datum WGS-84 (EPSG): 4240, $43^{\circ} 00' 37.84''$ N $12^{\circ} 25' 44.89''$ E. With reference to Fig. 6.30, the small red patch number one is containing the bridge used for processing data, which is shown in details in Fig. 6.31 (a) and (b). Fig. 6.32 is the sub-ROI representation consisting of the data input of the computational block number 5 depicted in Fig. 6.19 (a) and (b). in the sub-ROI am visible the bridge structure constituting of the collected energy and populating the range pixel line consisting in the spatial reference point and tracked by the pink layers L_1 and L_2 . The variance of the double-bounce layovered backscattered echoes is located inside the spatial gap contained by the blue layers L_3 and L_4 . The temporal trend of this layover scattering line is a function of the river water level. The trend of the estimated water levels are depicted in Fig. 6.33. The blue line represents the water-levels measured by the CSK satellite system and the red function represents the ground truths given by the ground-observation station.

5.5 Experiment case number two - case of study number three experimental results

This paragraph is devoted to showing results concerning the experimental case number three and referring to the case of study two. This new experiment shows the observation

of the Tiber river captured when it crosses the Italian capital city of Rome. Unfortunately for this case study, the author is not giving the ground-truths for comparison. Data will be provided in future researches. Fig. 6.35 (a) shows the geocoded SAR image where the ROI is visible by the red box tagged by the yellow number 1. The ROI is represented in detail by Fig. 6.35 (b) where the bridge is observed by an optical image and contoured by the same red box. The author used the double-bounce electromagnetic scattering effects generated by the *Guglielmo Marconi* bridge indicated by the yellow arrow which is geolocated on the following coordinates: datum WGS-84 (EPSG): 4240, $41^{\circ} 51' 36.10''$ N $12^{\circ} 28' 38.00''$ E. The optical representation of the *Guglielmo Marconi* bridge is showed in Fig. 6.36 (a). The temporal trend of the layered scattering trend which is a function of the river water level is depicted in Fig. 6.36 (b).

CHAPTER 6

Conclusions

The objective of this manuscript was to perform the precise measurement of rivers velocities using SAR. Today a worldwide database containing the historical and reliable data concerning the water surface speed of rivers is non-existent. This manuscript had the objective of contributing to solving this problem designing SAR processing techniques able to perform water flow velocity estimation. The problem of measuring such parameter is solved designing the ATI SAR geometry which is constituted of using two radars spatially distanced by a baseline extended in the azimuth direction. In the case of space-borne missions, it is unusual to perform ATI because the designation of real-time SAR observations spatially distanced by an along-track physical baseline is a difficult task. For several monocular space-borne SAR satellite systems, the refocusing of ATI observations from one raw data can be a problem because of the under-sampled nature of the received electromagnetic bursts. This phenomenon is practiced for onboard memory space saving which makes data appearing like a white random process, making interlaced Doppler bands completely disjoint. This phenomenon, after the range-Doppler focusing process, causes decorrelation when considering the ATI interferometric phase information retransmitted by distributed targets. Space-borne LOS velocity measurements could be taken into consideration only for small and very coherent targets and in any case located within the same radar resolution cell. This paper was proposing the application of two techniques for measuring the surface water velocities of rivers. The first method used the MCA which was applied in the Doppler domain and com-

bined to MCA-ATI-SAR was used to measure the range velocity component of water. For developing this technique some airborne full polarimetric SAR data observed by the uninhabited aerial vehicle synthetic aperture radar (UAVSAR) was processed. For developing the second technique, which is based on the magnitude analysis only where several COSMO-SkyMed data-set were used. This research was found to be suitable for finding excellent solutions of the experimental results thanks also to the high level of information which is embedded in the single SAR raw product.

Bibliography

- [1] Goldstein, Richard M., and H. A. Zebker. "Interferometric radar measurement of ocean surface currents." *Nature* 328.6132 (1987): 707. 3
- [2] Goldstein, R. M., Zebker, H. A., Barnett, T. P. (1989). Remote sensing of ocean currents. *Science*, 246(4935), 1282-1285. 3
- [3] R. Romeiser et al., "Current measurements by SAR along-track interferometry from a Space Shuttle," in *IEEE Transactions on Geoscience and Remote Sensing*, vol. 43, no. 10, pp. 2315-2324, Oct. 2005. doi: 10.1109/TGRS.2005.856116 3
- [4] Romeiser, R., Thompson, D. R. (2000). Numerical study on the along-track interferometric radar imaging mechanism of oceanic surface currents. *IEEE transactions on geoscience and remote sensing*, 38(1), 446-458. 4
- [5] Romeiser, R., Suchandt, S., Runge, H., Steinbrecher, U., Grunler, S. (2010). First analysis of TerraSAR-X along-track InSAR-derived current fields. *IEEE Transactions on Geoscience and Remote Sensing*, 48(2), 820-829. 4
- [6] Romeiser, R., Runge, H., Suchandt, S., Sprenger, J., Weilbeer, H., Sohrmann, A., Stammer, D. (2007). Current measurements in rivers by spaceborne along-track InSAR. *IEEE Transactions on Geoscience and Remote Sensing*, 45(12), 4019-4031. 3
- [7] J. F. Nouvel, P. Dubois-Fernandez, P. Kosuth and Y. Lasne, "Along Track Interferometry on Rhone River," *IGARSS 2008 - 2008 IEEE International Geoscience and Remote Sensing Symposium*, Boston, MA, 2008, pp. V - 495-V - 497. 4

- [8] Duk-jin Kim, W. M. Moon, D. Moller and D. A. Imel, "Measurements of ocean surface waves and currents using L- and C-band along-track interferometric SAR," in IEEE Transactions on Geoscience and Remote Sensing, vol. 41, no. 12, pp. 2821-2832, Dec. 2003. 4
- [9] F. Lombardini, F. Bordoni, F. Gini and L. Verrazzani, "Multibaseline ATI-SAR for robust ocean surface velocity estimation," in IEEE Transactions on Aerospace and Electronic Systems, vol. 40, no. 2, pp. 417-433, April 2004. 4
- [10] M. A. Sletten, "An analysis of gradient-induced distortion in ATI-SAR imagery of surface currents," in IEEE Transactions on Geoscience and Remote Sensing, vol. 44, no. 7, pp. 1995-2002, July 2006. 5
- [11] S. J. Frasier and A. J. Camps, "Dual-beam interferometry for ocean surface current vector mapping," in IEEE Transactions on Geoscience and Remote Sensing, vol. 39, no. 2, pp. 401-414, Feb 2001. 5
- [12] R. Siegmund, Mingquan Bao, S. Lehner and R. Mayerle, "First demonstration of surface currents imaged by hybrid along- and cross-track interferometric SAR," in IEEE Transactions on Geoscience and Remote Sensing, vol. 42, no. 3, pp. 511-519, March 2004. 5
- [13] Michel, R., Avouac, J. P., Taboury, J. (1999). Measuring ground displacements from SAR amplitude images: Application to the Landers earthquake. *Geophysical Research Letters*, 26(7), 875-878. 7
- [14] Strozzi, T., Luckman, A., Murray, T., Wegmüller, U., Werner, C. L. (2002). Glacier motion estimation using SAR offset-tracking procedures. *IEEE Transactions on Geoscience and Remote Sensing*, 40(11), 2384-2391. 7

- [15] Casu, F., Manconi, A., Pepe, A., Lanari, R. (2011). Deformation time-series generation in areas characterized by large displacement dynamics: The SAR amplitude pixel-offset SBAS technique. *IEEE Transactions on Geoscience and Remote Sensing*, 49(7), 2752-2763. 7
- [16] Casu, F., Manconi, A. (2016). Four-dimensional surface evolution of active rifting from spaceborne SAR data. *Geosphere*, 12(3), 697-705. 7
- [17] Nitti, D. O., Hanssen, R. F., Refice, A., Bovenga, F., Nutricato, R. (2011). Impact of DEM-assisted coregistration on high-resolution SAR interferometry. *IEEE Transactions on Geoscience and Remote Sensing*, 49(3), 1127-1143. 7
- [18] PAVELSKY, Tamlin M.; SMITH, Laurence C. RivWidth: A software tool for the calculation of river widths from remotely sensed imagery. *IEEE Geoscience and Remote Sensing Letters*, 2008, 5.1: 70-73. 6
- [19] CHICKADEL, C. Chris, et al. Infrared-based measurements of velocity, turbulent kinetic energy, and dissipation at the water surface in a tidal river. *IEEE Geoscience and Remote Sensing Letters*, 2011, 8.5: 849-853. 6
- [20] TARPANELLI, Angelica, et al. Coupling MODIS and radar altimetry data for discharge estimation in poorly gauged river basins. *IEEE Journal of Selected Topics in Applied Earth Observations and Remote Sensing*, 2015, 8.1: 141-148. 6
- [21] STROKINA, Nataliya, et al. Joint estimation of bulk flow velocity and angle using a lateral line probe. *IEEE Transactions on Instrumentation and Measurement*, 2016, 65.3: 601-613. 6
- [22] F. Biondi, "Low rank plus sparse decomposition of synthetic aperture radar data for maritime surveillance," 2016 4th International Workshop on Compressed Sens-

ing Theory and its Applications to Radar, Sonar and Remote Sensing (CoSeRa), Aachen, 2016, pp. 75-79.

- [23] Duque, Sergi, et al. "Absolute height estimation using a single TerraSAR-X staring spotlight acquisition." *IEEE Geoscience and Remote Sensing Letters* 12.8 (2015): 1735-1739. [7](#), [13](#)
- [24] Mâcotivier, F. "Diffusivelike buffering and saturation of large rivers." *Physical Review E* 60.5 (1999): 5827. [7](#), [20](#)
- [25] Costa, J. E., Cheng, R. T., Haeni, F. P., Melcher, N., Spicer, K. R., Hayes, E., ... Barrick, D. (2006). Use of radars to monitor stream discharge by noncontact methods. *Water Resources Research*, 42(7). [8](#)
- [26] Chiu, C. L. (1989). Velocity distribution in open channel flow. *Journal of Hydraulic Engineering*, 115(5), 576-594. [8](#)
- [27] Chiu, C. L., Hsu, S. M., Tung, N. C. (2005). Efficient methods of discharge measurements in rivers and streams based on the probability concept. *Hydrological Processes: An International Journal*, 19(20), 3935-3946. [8](#)
- [28] Plant, W. J., Wright, J. W. (1980). Phase speeds of upwind and downwind traveling short gravity waves. *Journal of Geophysical Research: Oceans*, 85(C6), 3304-3310. [8](#)
- [29] Plant, W. J., Keller, W. C. (1990). Evidence of Bragg scattering in microwave Doppler spectra of sea return. *Journal of Geophysical Research: Oceans*, 95(C9), 16299-16310. [8](#)
- [30] Plant, W. J., Keller, W. C., Hesany, V., Hayes, K., Hoppel, K. W., Blanc, T. V. (1998). Measurements of the marine boundary layer from an airship. *Journal of Atmospheric and Oceanic Technology*, 15(6), 1433-1458. [9](#)

- [31] Plant, W. J., Keller, W. C., Hayes, K., Spicer, K. (2005). Streamflow properties from time series of surface velocity and stage. *Journal of Hydraulic Engineering*, 131(8), 657-664. [9](#)
- [32] Plant, W. J., Keller, W. C., Hayes, K. (2005). Simultaneous measurement of ocean winds and waves with an airborne coherent real aperture radar. *Journal of Atmospheric and Oceanic Technology*, 22(7), 832-846. [9](#)
- [33] Plant, W. J., Keller, W. C., Hayes, K. (2005). Measurement of river surface currents with coherent microwave systems. *IEEE Transactions on Geoscience and Remote Sensing*, 43(6), 1242-1257. [6](#), [10](#)
- [34] Bass, F., Fuks, I., Kalmykov, A., Ostrovsky, I., Rosenberg, A. (1968). Very high frequency radiowave scattering by a disturbed sea surface Part I: Scattering from a slightly disturbed boundary. *IEEE Transactions on Antennas and Propagation*, 16(5), 554-559. [10](#)
- [35] Bass, F., Fuks, I., Kalmykov, A., Ostrovsky, I., Rosenberg, A. (1968). Very high frequency radiowave scattering by a disturbed sea surface Part II: Scattering from an actual sea surface. *IEEE Transactions on Antennas and Propagation*, 16(5), 560-568. [10](#)
- [36] Hasselmann, K., Raney, R. K., Plant, W. J., Alpers, W., Shuchman, R. A., Lyzenga, D. R., ... Tucker, M. J. (1985). Theory of synthetic aperture radar ocean imaging: A MARSEN view. *Journal of Geophysical Research: Oceans*, 90(C3), 4659-4686. [10](#)
- [37] Melcher, N. B., Costa, J. E., Haeni, F. P., Cheng, R. T., Thurman, E. M., Bur sink, M., ... Hayes, K. (2002). River discharge measurements by using helicopter-mounted radar. *Geophysical Research Letters*, 29(22), 41-1. [10](#)

- [38] Alpers, W. R., Ross, D. B., Rufenach, C. L. (1981). On the detectability of ocean surface waves by real and synthetic aperture radar. *Journal of Geophysical Research: Oceans*, 86(C7), 6481-6498. [11](#)
- [39] Alpers, W., Hasselmann, K. (1978). The two-frequency microwave technique for measuring ocean-wave spectra from an airplane or satellite. *Boundary-Layer Meteorology*, 13(1-4), 215-230. [11](#)

List of captions

Figure 6.1. Experiment case number one - computational scheme.

Figure 6.2. (a): Stripmap-like SAR acquisition geometry. (b): Time-frequency designation of the azimuth matched filter.

Figure 6.3. Multi-chromatic analysis frequency allocation strategy.

Figure 6.4. (a): Frequency allocation plane. (b): Spectrum of the SAR raw data.

Figure 6.5. Experiment case number one - case study one full-polarimetric SAR result.

Figure 6.6. Experiment case number one - case study two full-polarimetric SAR result.

Figure 6.7. S11 polarimetric channel SLC SAR of the study-case number one river.

Figure 6.8. S11 polarimetric channel SLC SAR of the study-case number two river.

Figure 6.9. S11 polarimetric channel SLC SAR of the study-case number two river.

Figure 6.10. Line one river velocity profile of the study-case number two.

Figure 6.11. Full-polarimetric SLC data representation for data validation.

Figure 6.12. (a): magnitude intra-chromatic coherence. (b): phase of the intra-chromatic coherence.

Figure 6.13. ATI results. (a): large-swath velocity map. (b): detailed velocity map.

Figure 6.14. Line one river velocity profile of the validation case study.

Figure 6.15. Line one river velocity profile of the validation case study.

Figure 6.17. Line one river velocity profile of the validation case study.

Figure 6.18. Geometry of the rivers water-level estimation system concerning the experiment case number two. (a): Schematic representation in the range-azimuth representation plane. (b): Geometric scheme in the range-height reference plane.

Figure 6.19. Computational scheme concerning the experiment case number two. (a): General representation. (b): Detailed representation of the computational block number 5 concerning the range-shifts to water velocities conversion.

Figure 6.20. Experiment case number two - case of study number one location.

Figure 6.21. Experiment case number two - case of study number one footprints.

Figure 6.22. Experiment case number two - case of study number one ROI.

Figure 6.23. Experiment case number two - case of study number one SLC representation.

Figure 6.24. Experiment case number two - case of study number one. (a): South-East view. (b): South-East view.

Figure 6.25. Experiment case number two - case of study number one sub-ROI representation.

Figure 6.26. River water-levels heights. (red): Estimated by CSK. (blue): ground truths.

Figure 6.26. River water-levels heights errors. (blue): measurement errors existing between the CSK observations versus ground-truths (no average). (red): Measurement errors existing between the CSK observations versus ground-truths (average window of 5 observations). (black): Measurement errors existing between the CSK observations versus ground-truths (average window of 10 observations).

Figure 6.29. Experiment case number two - case of study number two SAR footprints.

Figure 6.30. Experiment case number two - case of study number two SLC representation.

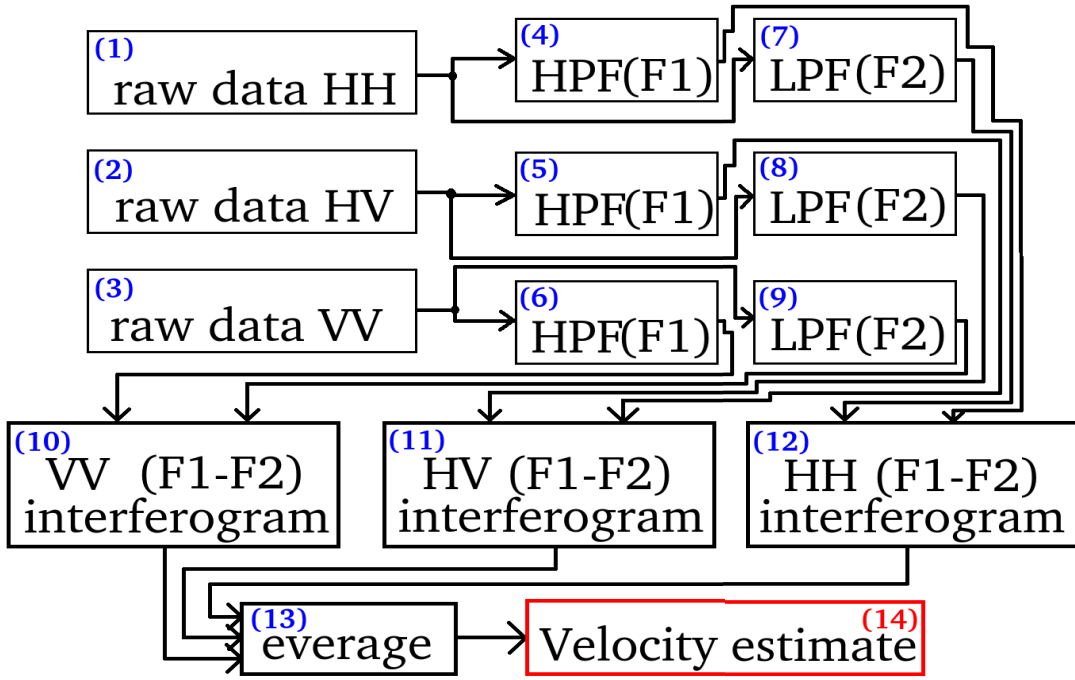


Fig. 6.1: Experiment case number one - computational scheme.

Figure 6.31. Experiment case number two - case of study number two. (a): South-East view. (b): South-East view.

Figure 6.32. Experiment case number two - case of study number two sub-ROI representation.

Figure 6.33. River water-levels heights. (red): Estimated by CSK. (blue): ground truths.

Figure 6.34. River water-levels heights errors. (blue): measurement errors existing between the CSK observations versus ground-truths (no average). (red): Measurement errors existing between the CSK observations versus ground-truths (average window of 5 observations). (black): Measurement errors existing between the CSK observations versus ground-truths (average window of 10 observations).

Figure 6.35. Geocoded SAR images.

Figure 6.36. (a): Marconi bridge located in Rome. (b): Estimated velocities.

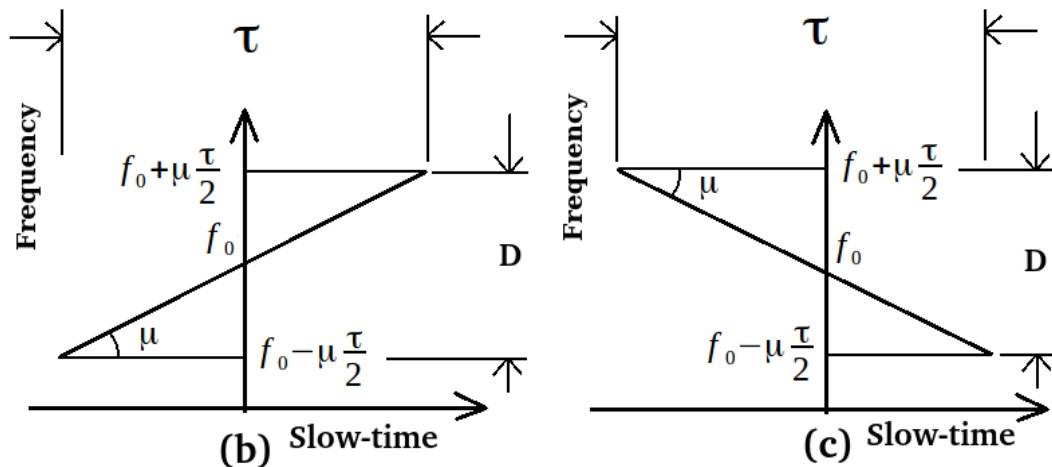
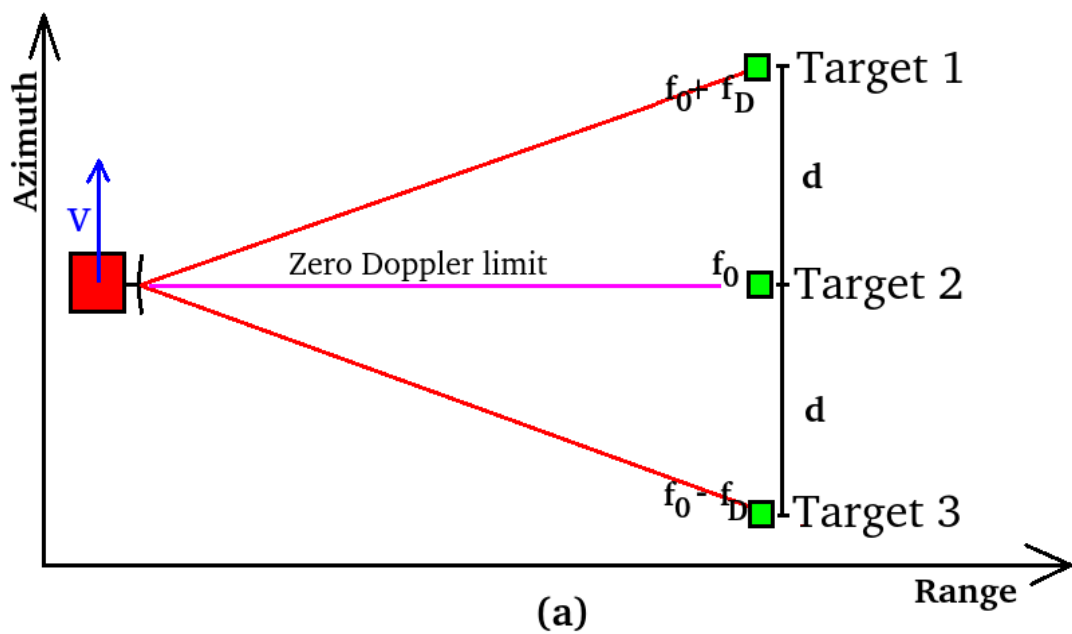


Fig. 6.2: (a):Stripmap-like SAR acquisition geometry. (b): Time-frequency designation of the azimuth matched filter.

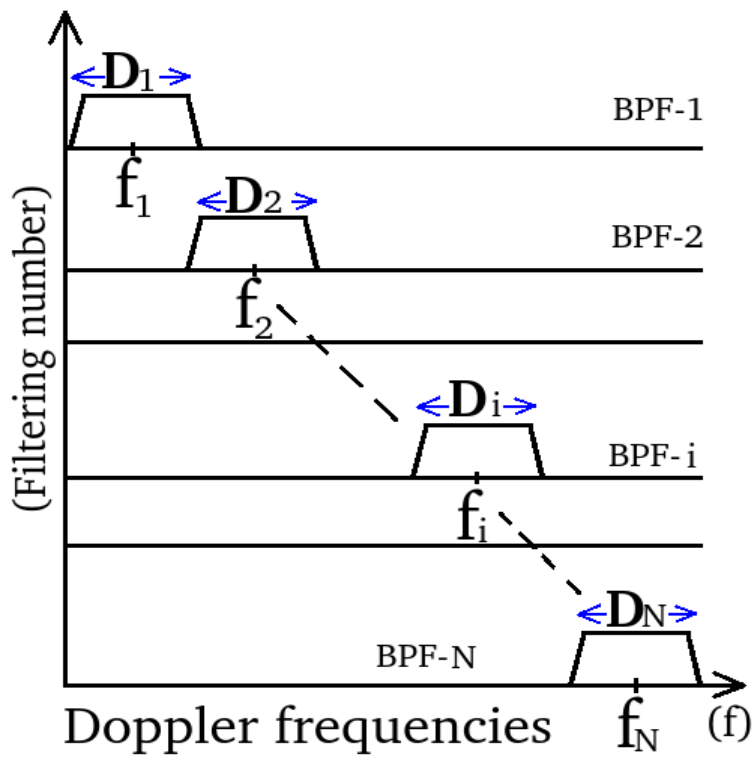


Fig. 6.3: Multi-chromatic analysis frequency allocation strategy.

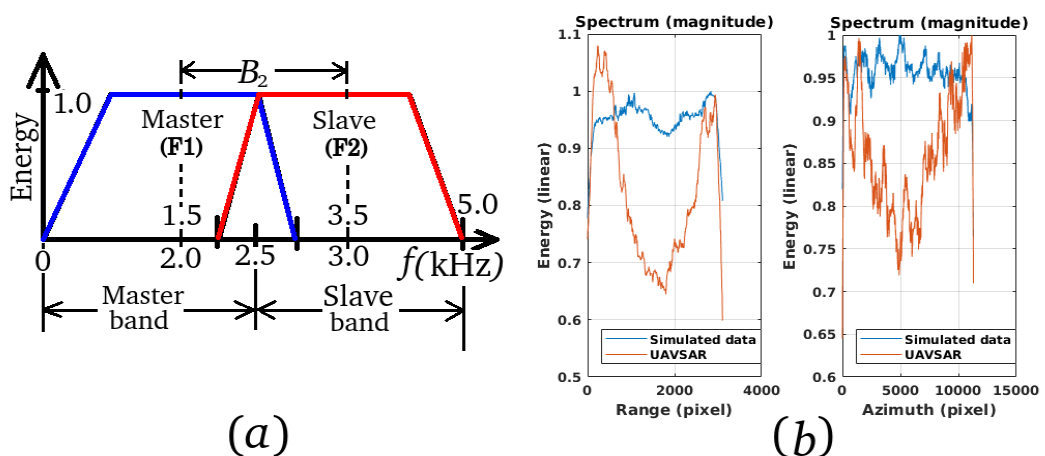


Fig. 6.4: (a): Frequency allocation plane. (b): Spectrum of the SAR raw data.

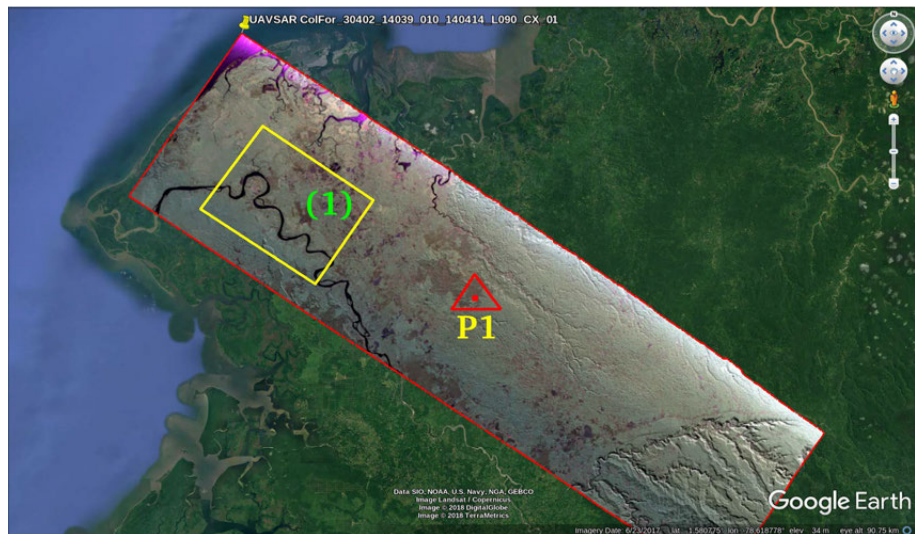


Fig. 6.5: Experiment case number one - case study one full-polarimetric SAR result.

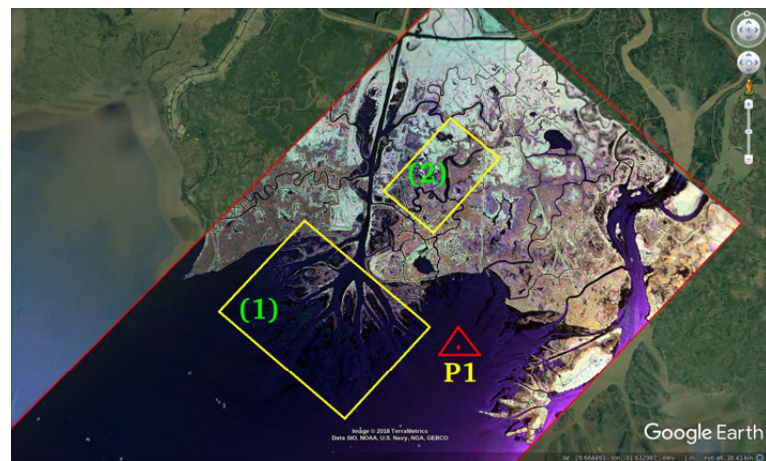


Fig. 6.6: Experiment case number one - case study two full-polarimetric SAR result.

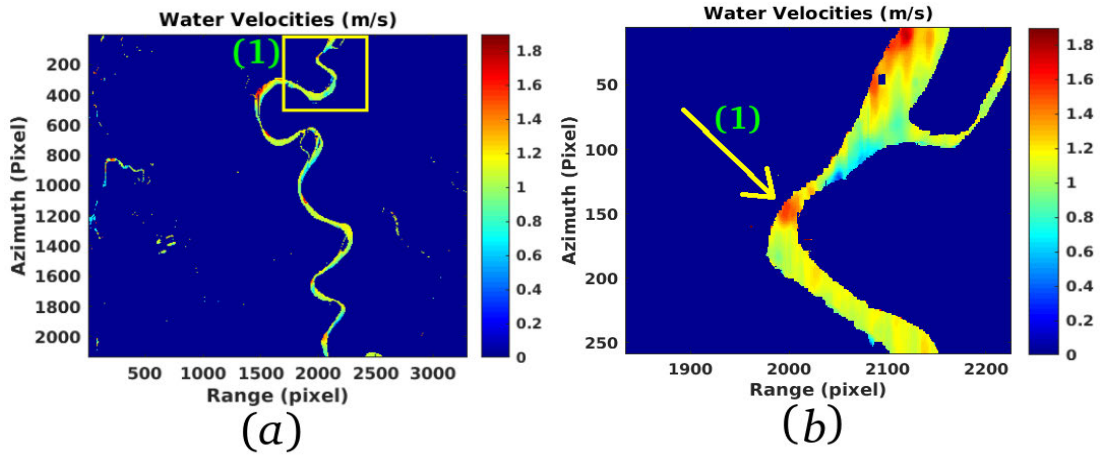


Fig. 6.7: S11 polarimetric channel SLC SAR of the study-case number one river.

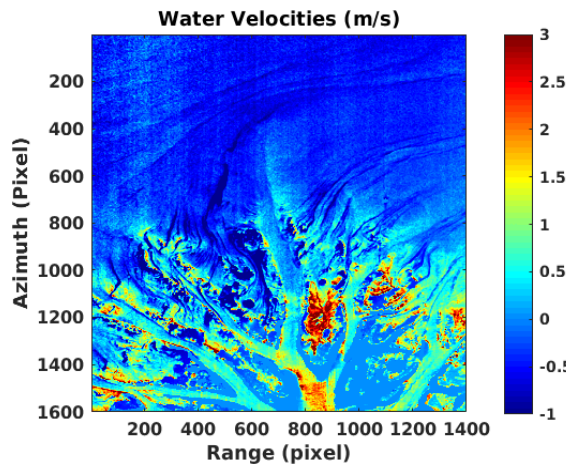


Fig. 6.8: S11 polarimetric channel SLC SAR of the study-case number two river.

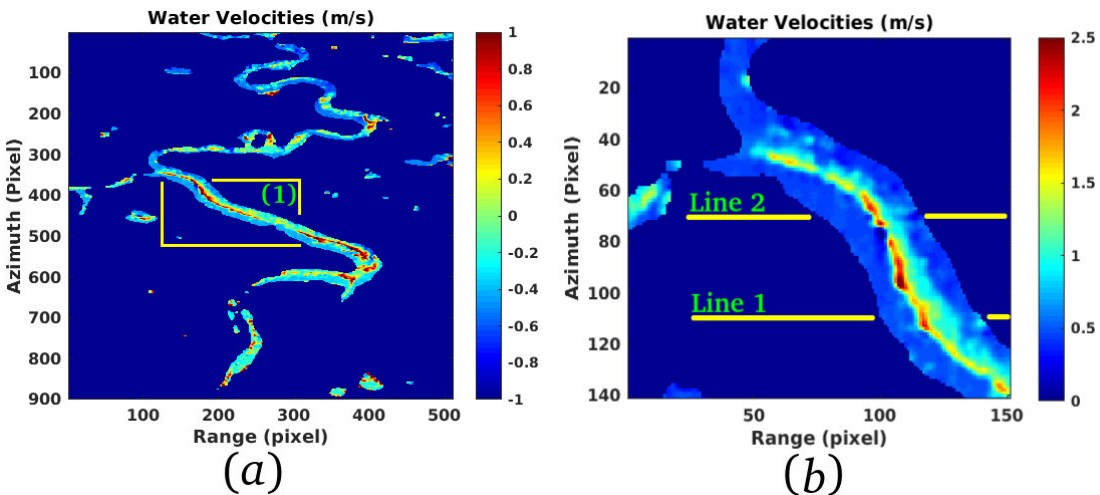


Fig. 6.9: S11 polarimetric channel SLC SAR of the study-case number two river.

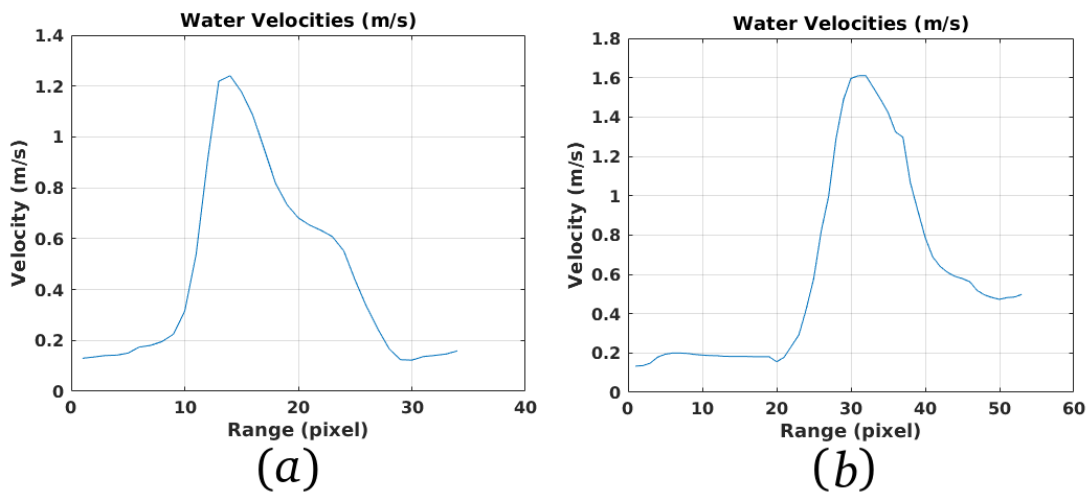


Fig. 6.10: Line one river velocity profile of the study-case number two.

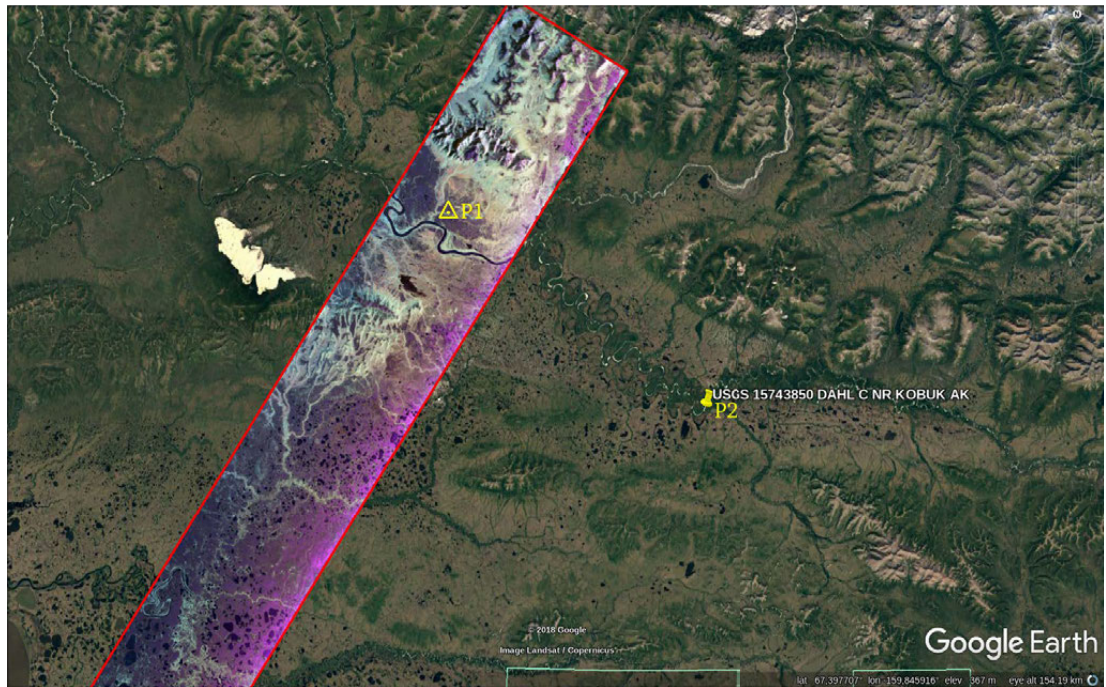


Fig. 6.11: Full-polarimetric SLC data representation for data validation.

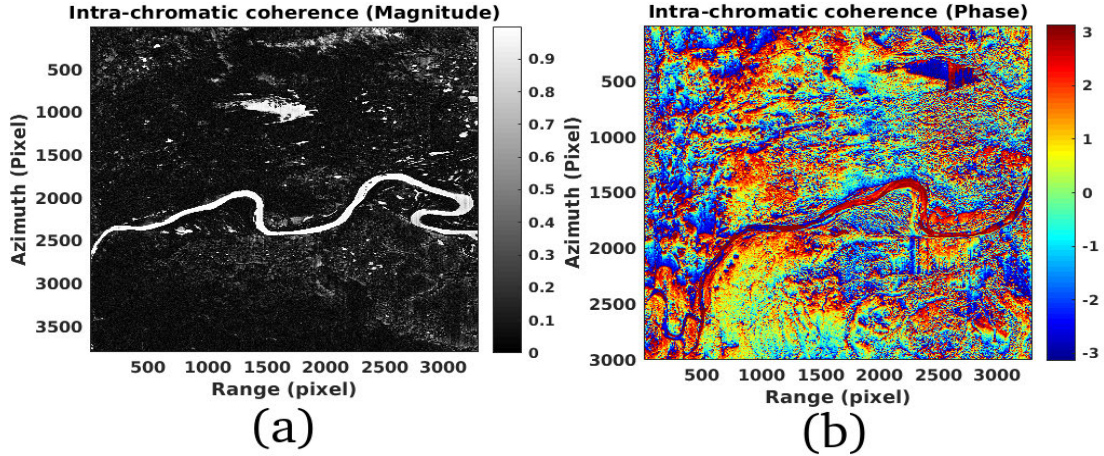


Fig. 6.12: (a): magnitude intra-chromatic coherence. (b): phase of the intra-chromatic coherence.

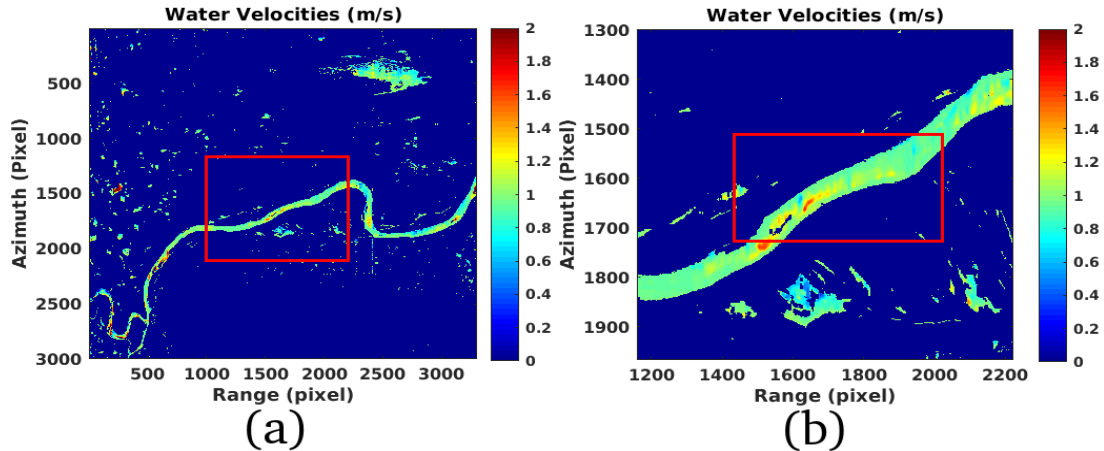


Fig. 6.13: ATI results. (a): large-swath velocity map. (b): detailed velocity map.

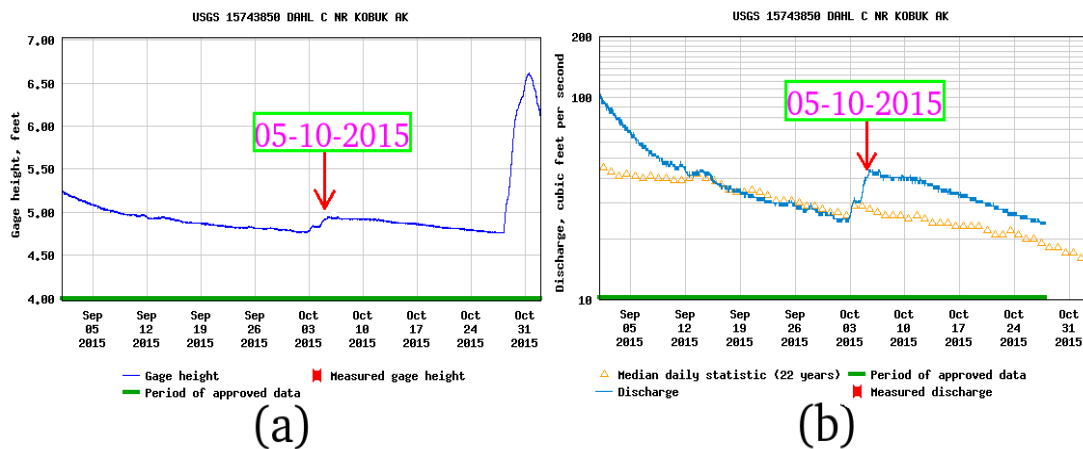


Fig. 6.14: Line one river velocity profile of the validation case study.

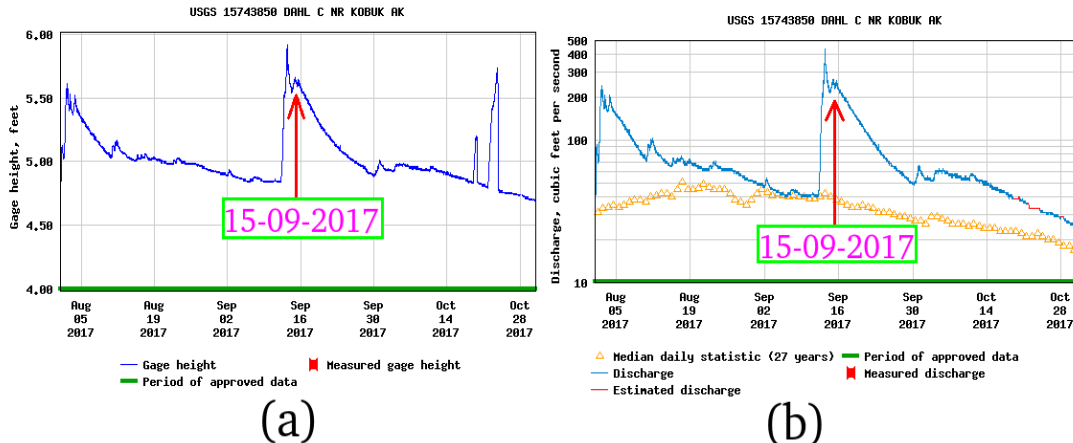


Fig. 6.15: Line one river velocity profile of the validation case study.

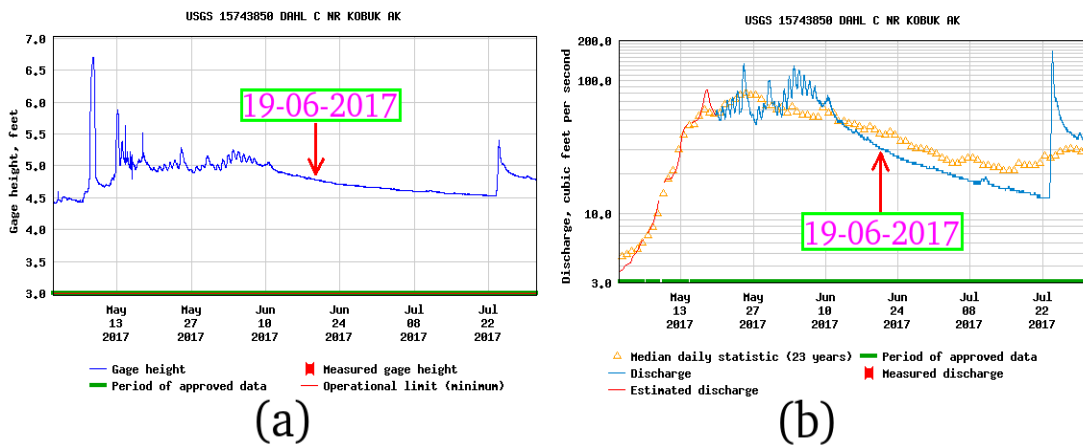


Fig. 6.16: Line one river velocity profile of the validation case study.

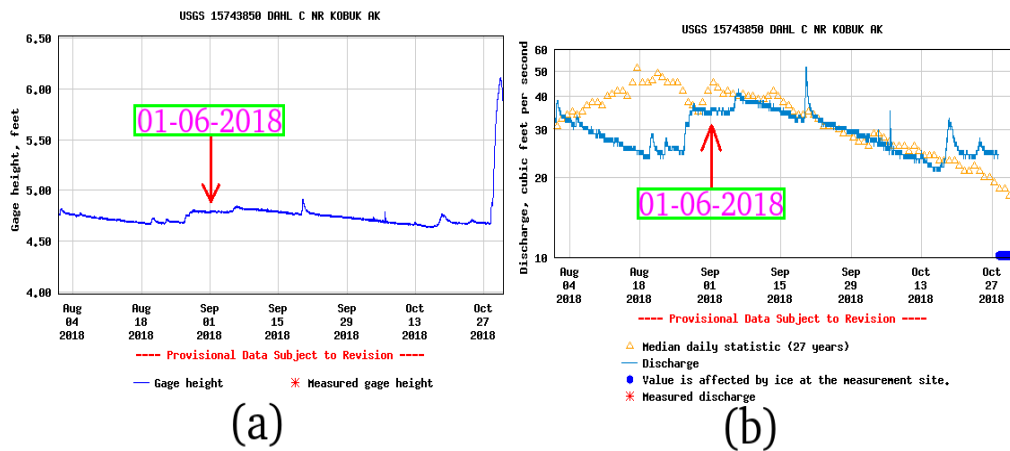


Fig. 6.17: Line one river velocity profile of the validation case study.

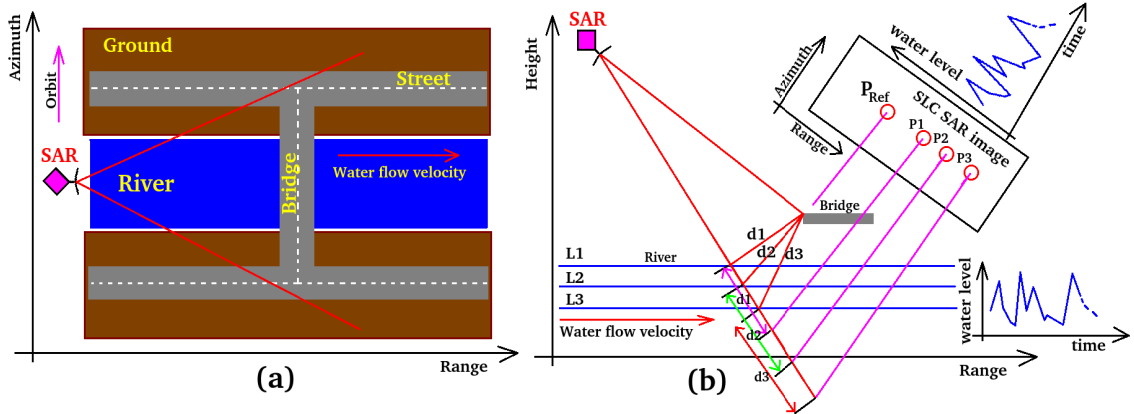


Fig. 6.18: Geometry of the rivers water-level estimation system concerning the experiment case number two. (a): Schematic representation in the range-azimuth representation plane. (b): Geometric scheme in the range-height reference plane.

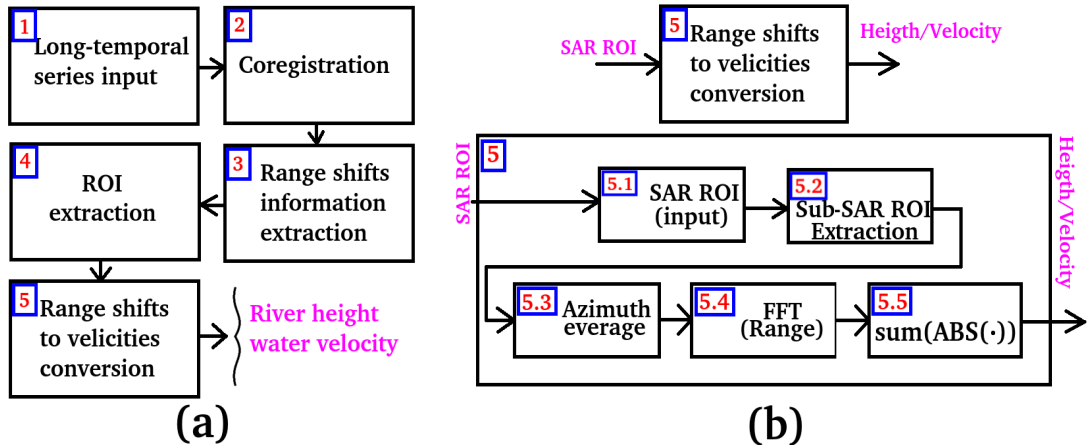


Fig. 6.19: Computational scheme concerning the experiment case number two. (a): General representation. (b): Detailed representation of the computational block number 5 concerning the range-shifts to water velocities conversion.

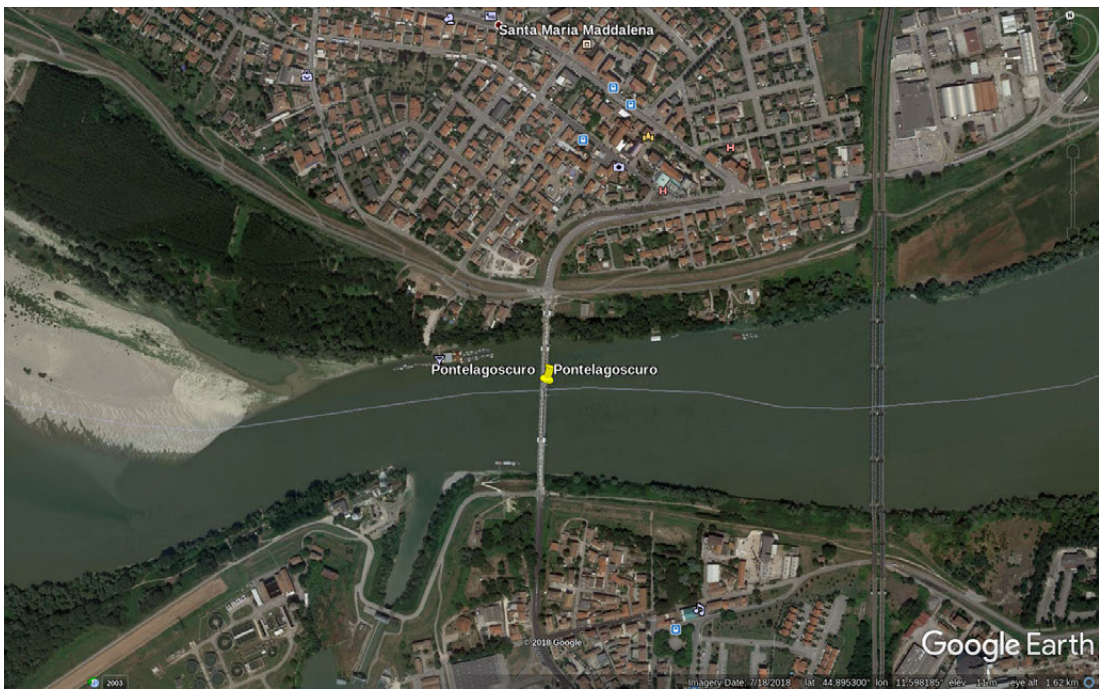


Fig. 6.20: Experiment case number two - case of study number one location.

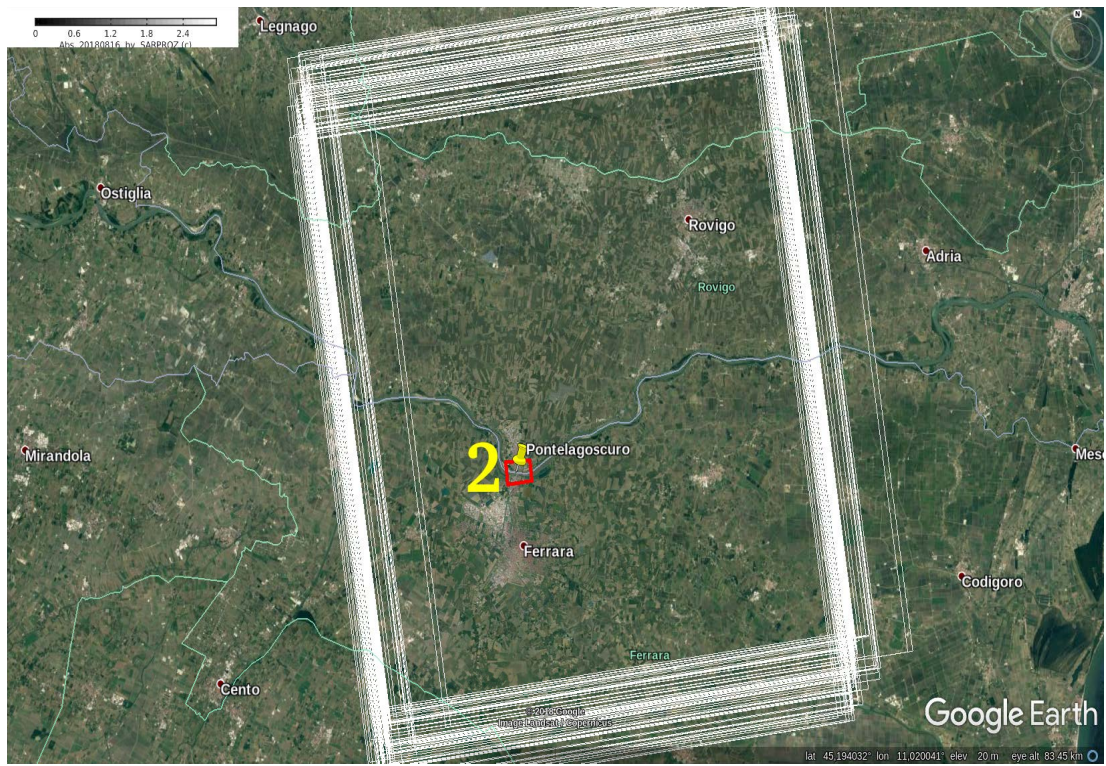


Fig. 6.21: Experiment case number two - case of study number one footprints.

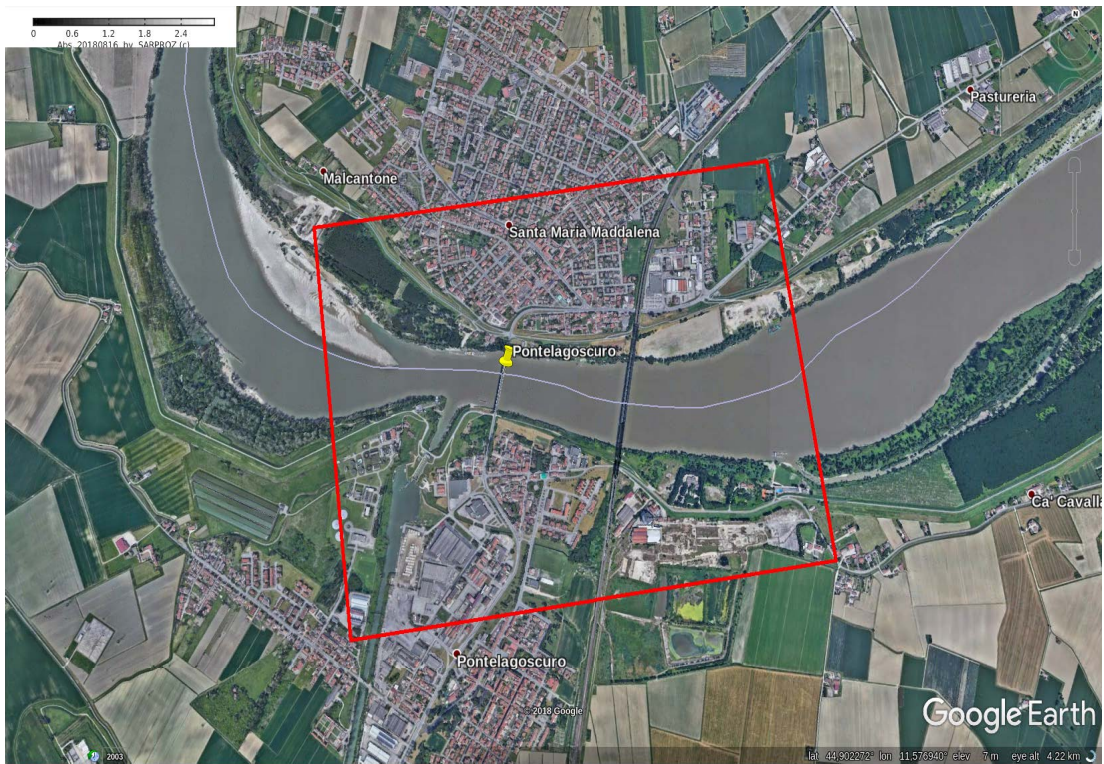


Fig. 6.22: Experiment case number two - case of study number one ROI.

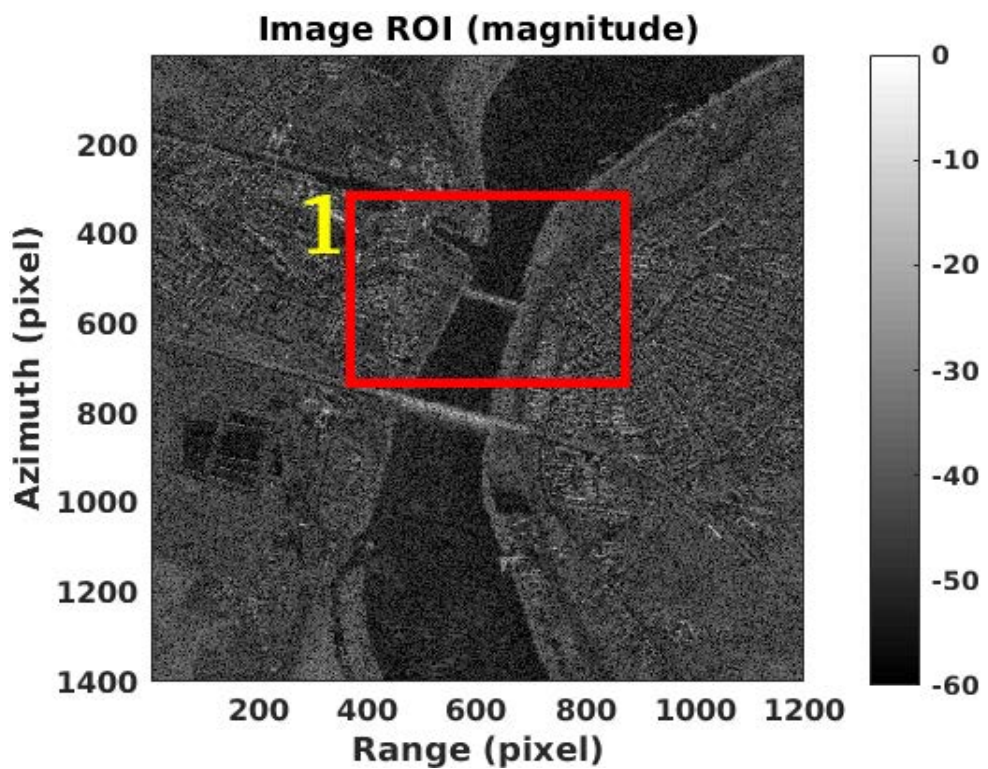


Fig. 6.23: Experiment case number two - case of study number one SLC representation.



(a)

(b)

Fig. 6.24: Experiment case number two - case of study number one. (a): South-East view. (b): South-East view.

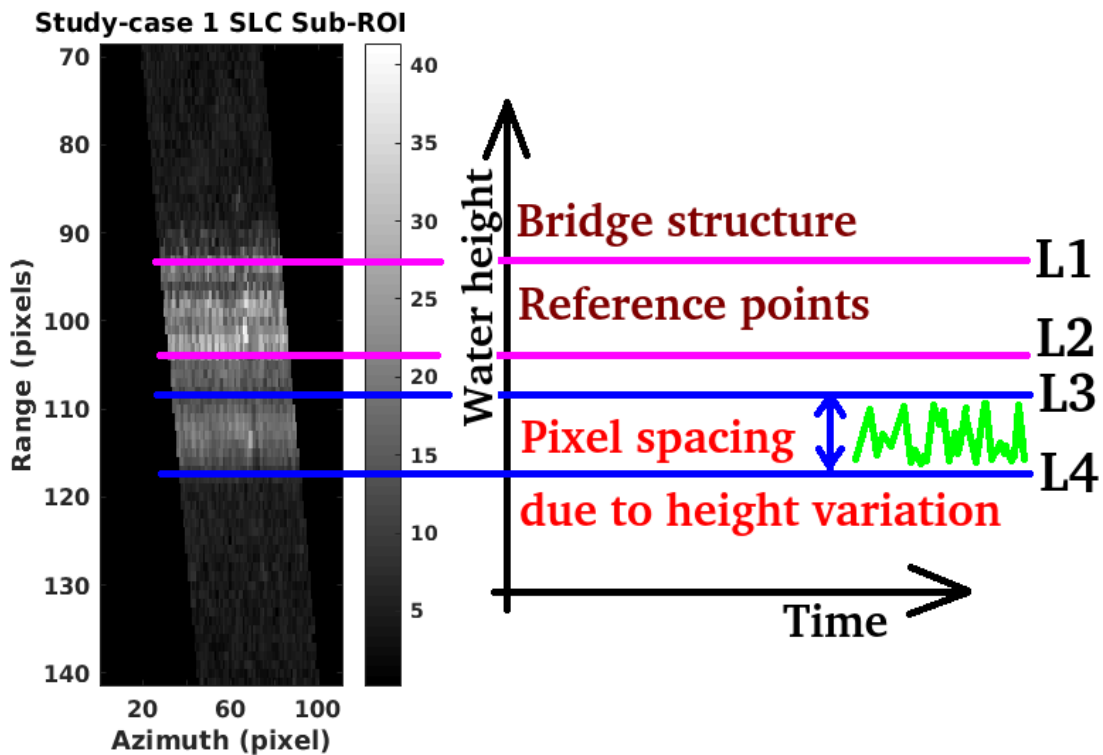


Fig. 6.25: Experiment case number two - case of study number one sub-ROI representation.

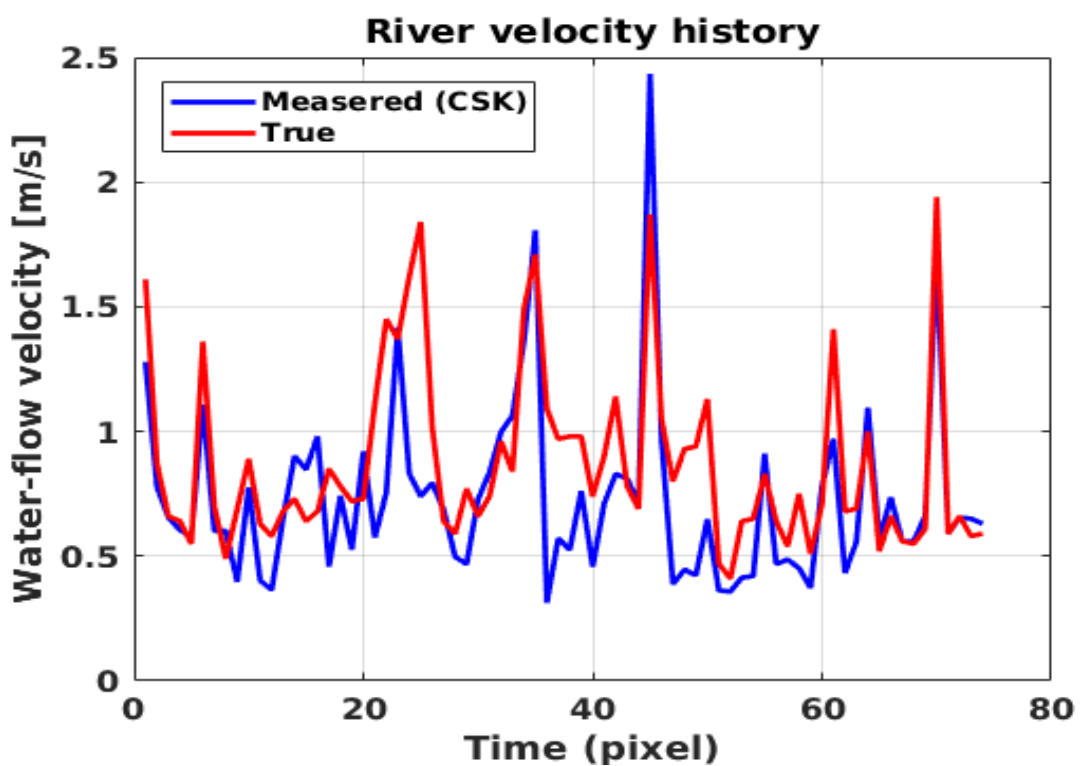


Fig. 6.26: River water-levels heights. (red): Estimated by CSK. (blue): ground-truths.

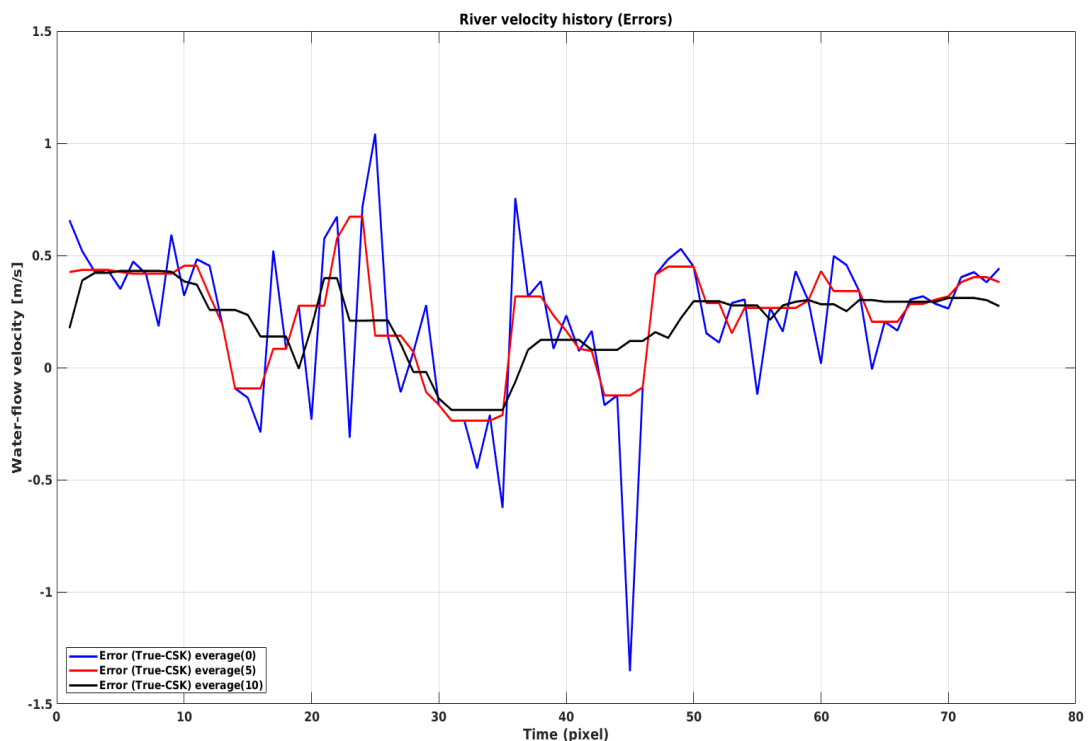


Fig. 6.27: River water-levels heights errors. (blue): measurement errors existing between the CSK observations versus ground-truths (no average). (red): Measurement errors existing between the CSK observations versus ground-truths (average window of 5 observations). (black): Measurement errors existing between the CSK observations versus ground-truths (average window of 10 observations).

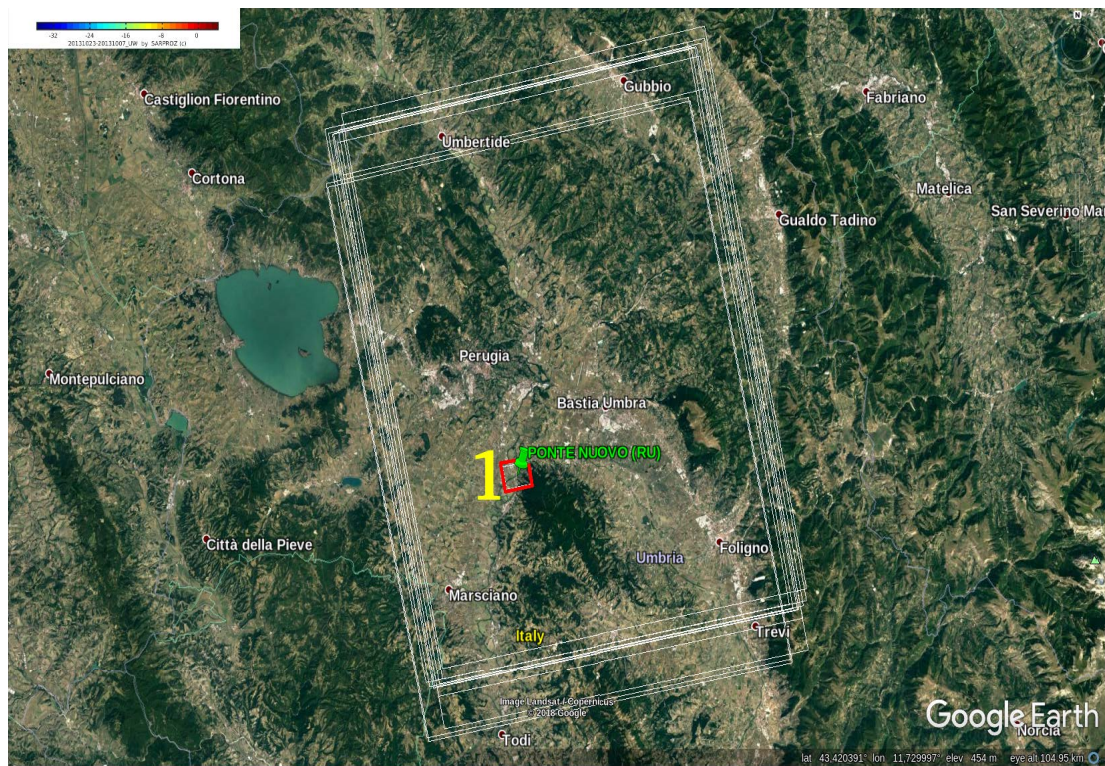


Fig. 6.28: Experiment case number two - case of study number two SAR footprints.

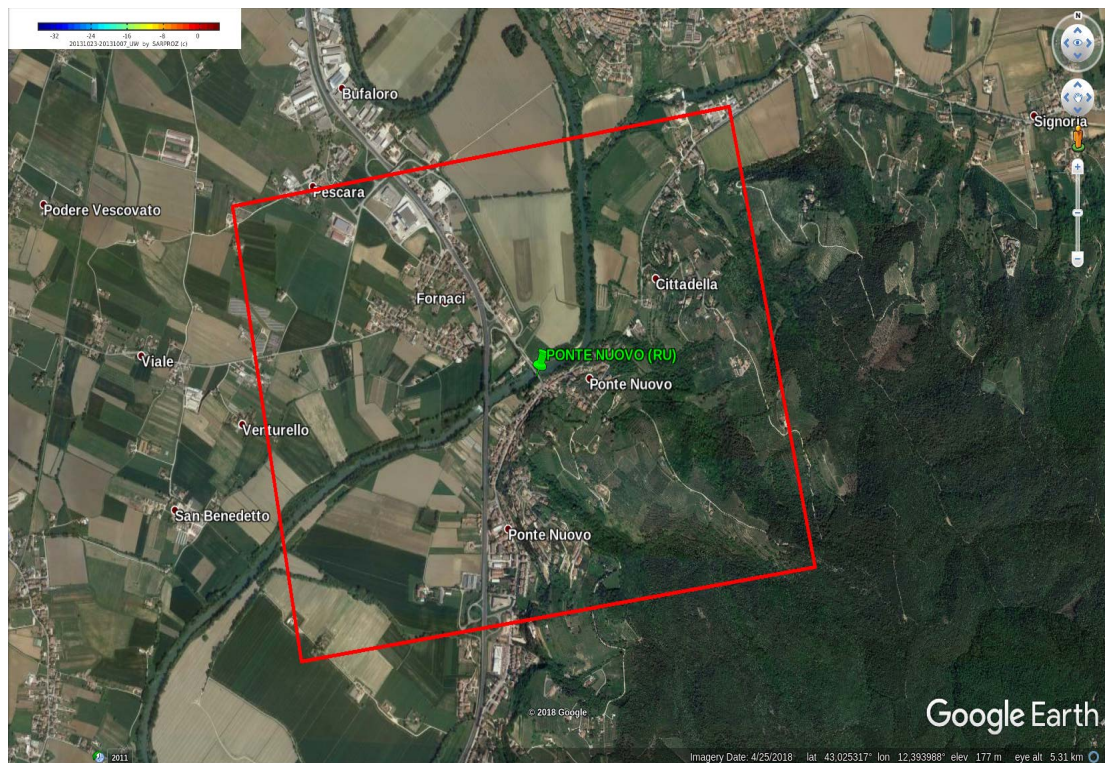


Fig. 6.29: Experiment case number two - case of study number two ROI.

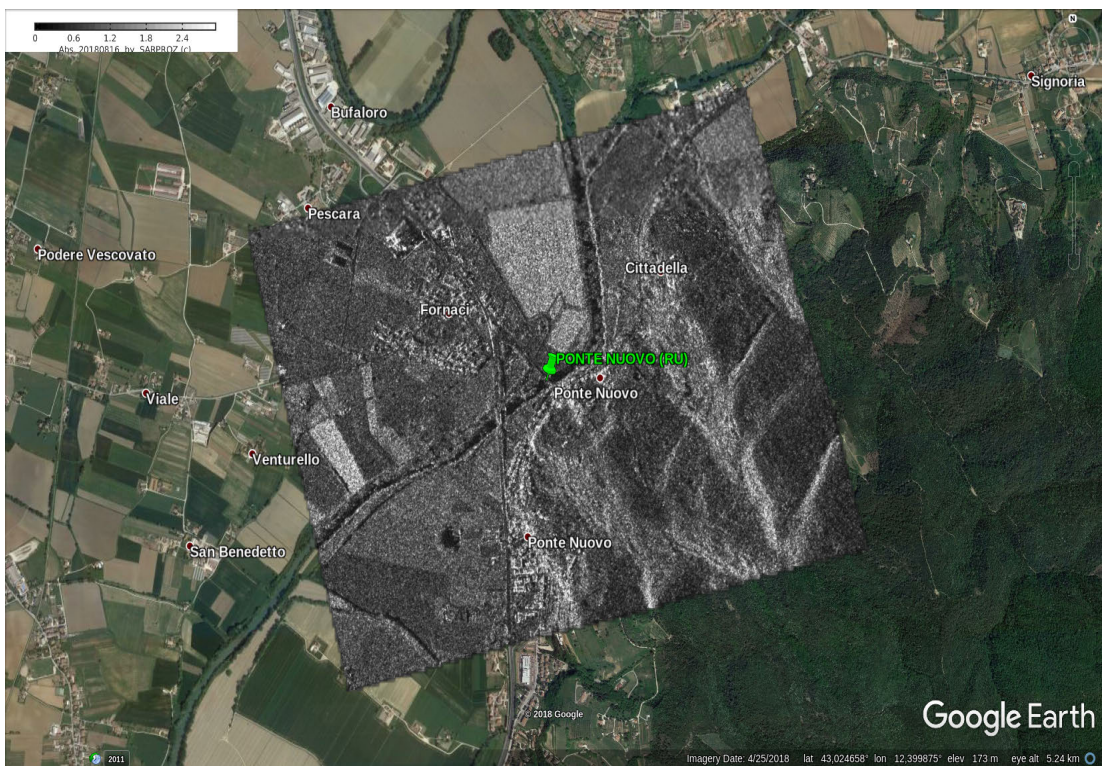


Fig. 6.30: Experiment case number two - case of study number two SLC representation.

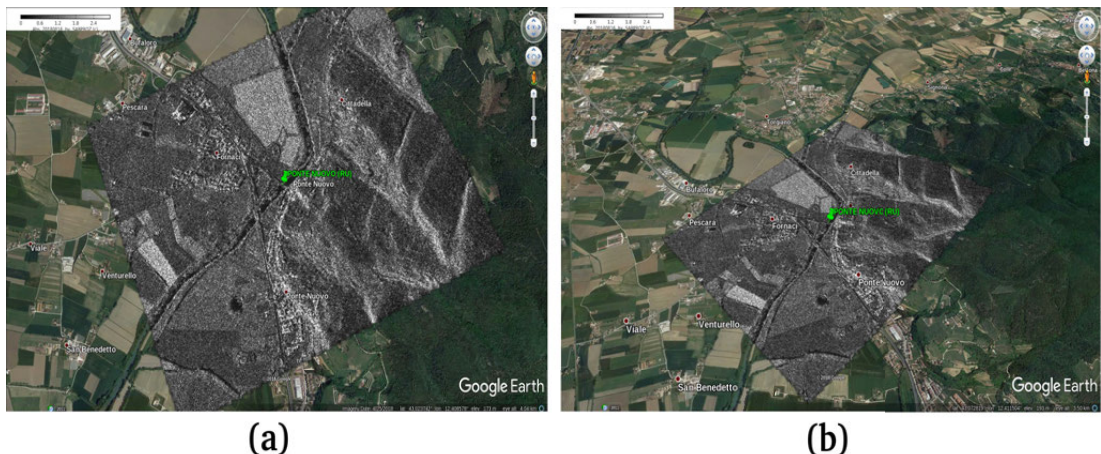


Fig. 6.31: Experiment case number two - case of study number two. (a): South-East view. (b): South-East view.

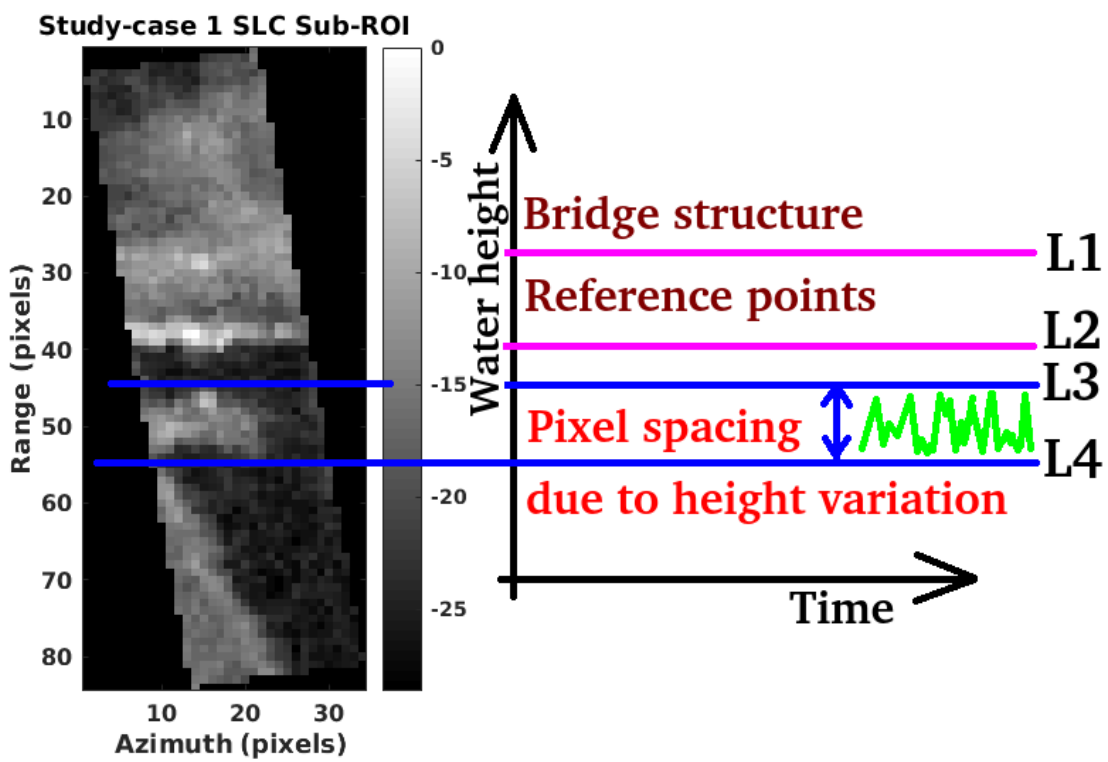


Fig. 6.32: Experiment case number two - case of study number two sub-ROI representation.

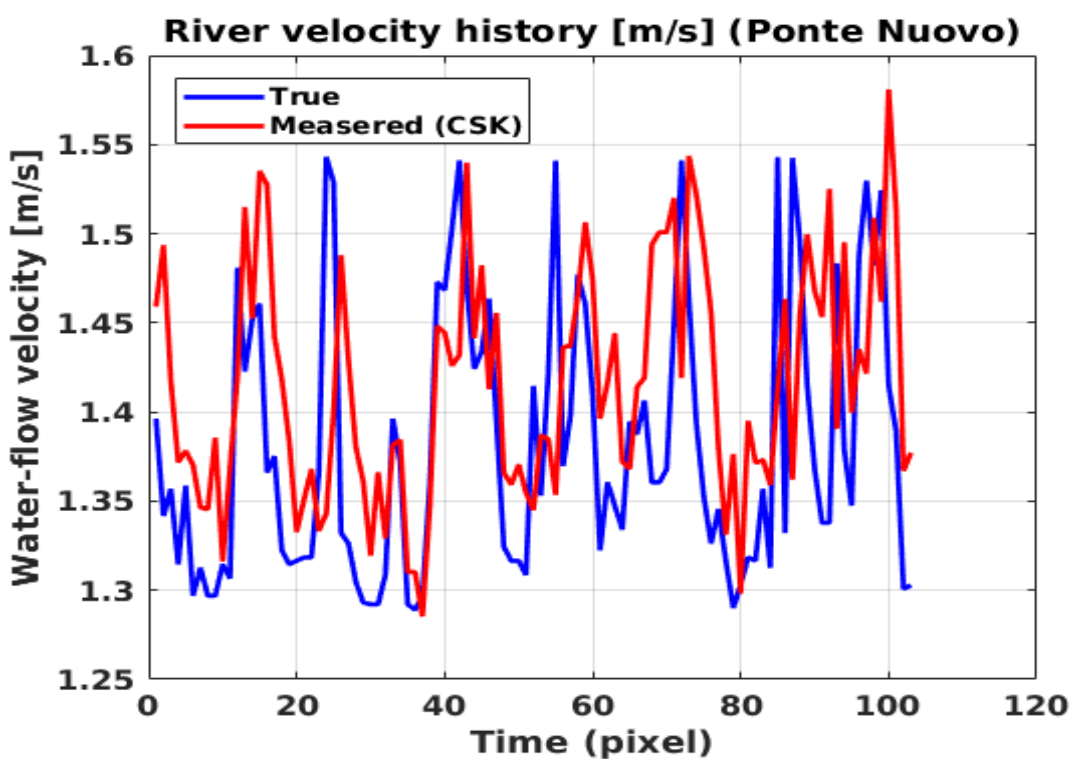


Fig. 6.33: River water-levels heights. (red): Estimated by CSK. (blue): ground-truths.

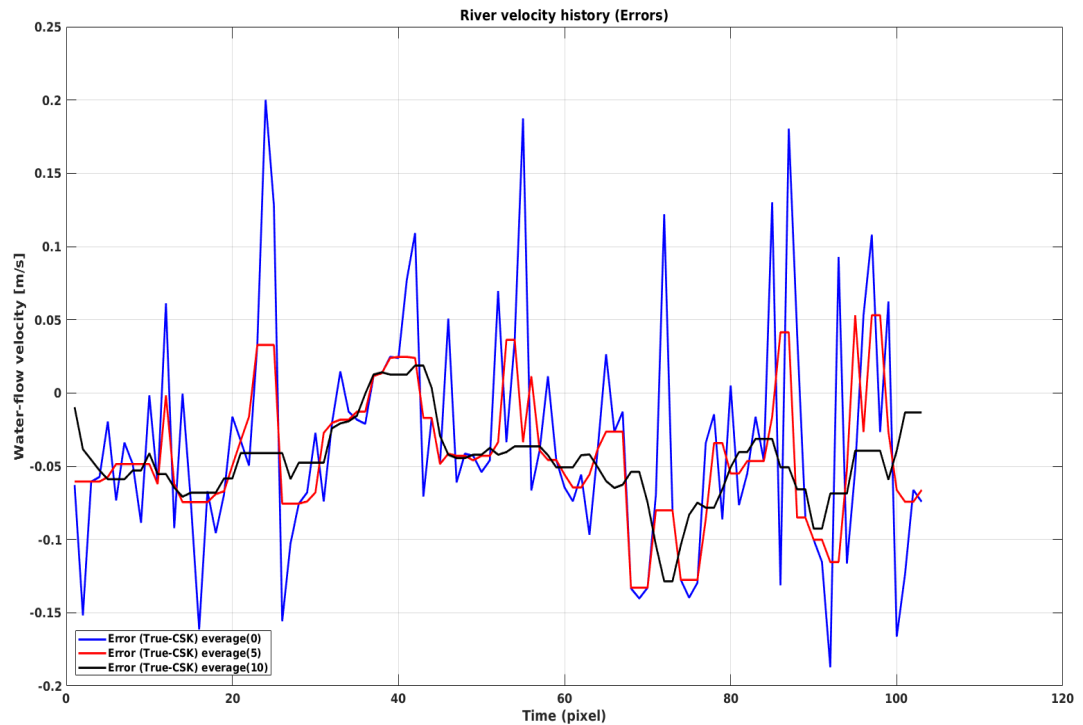
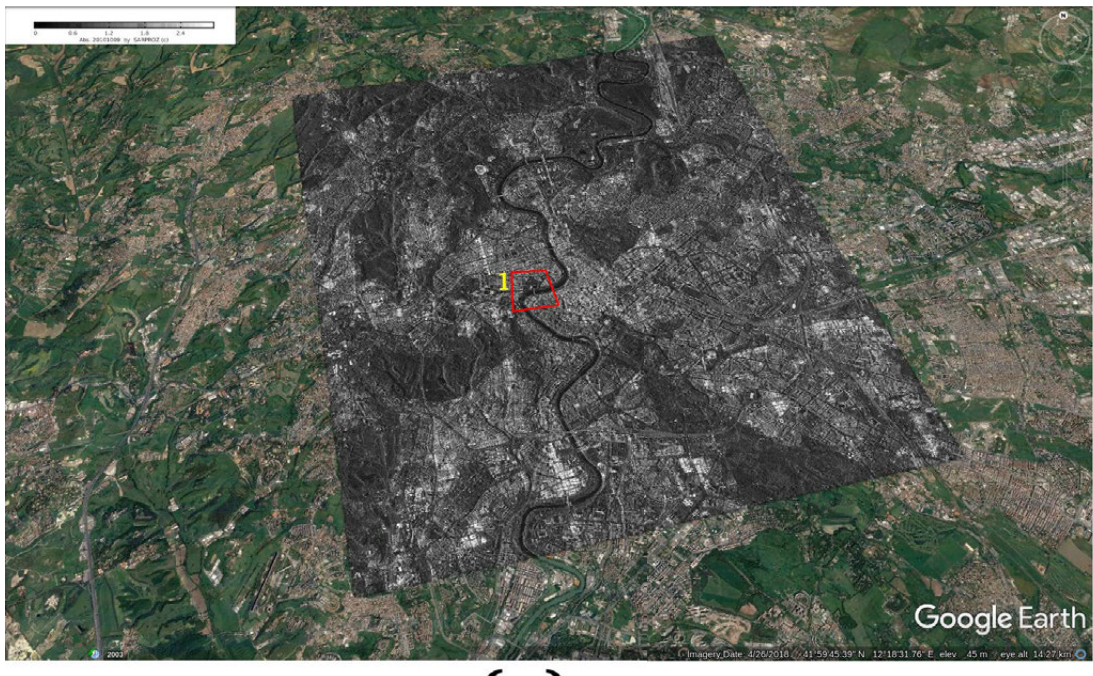
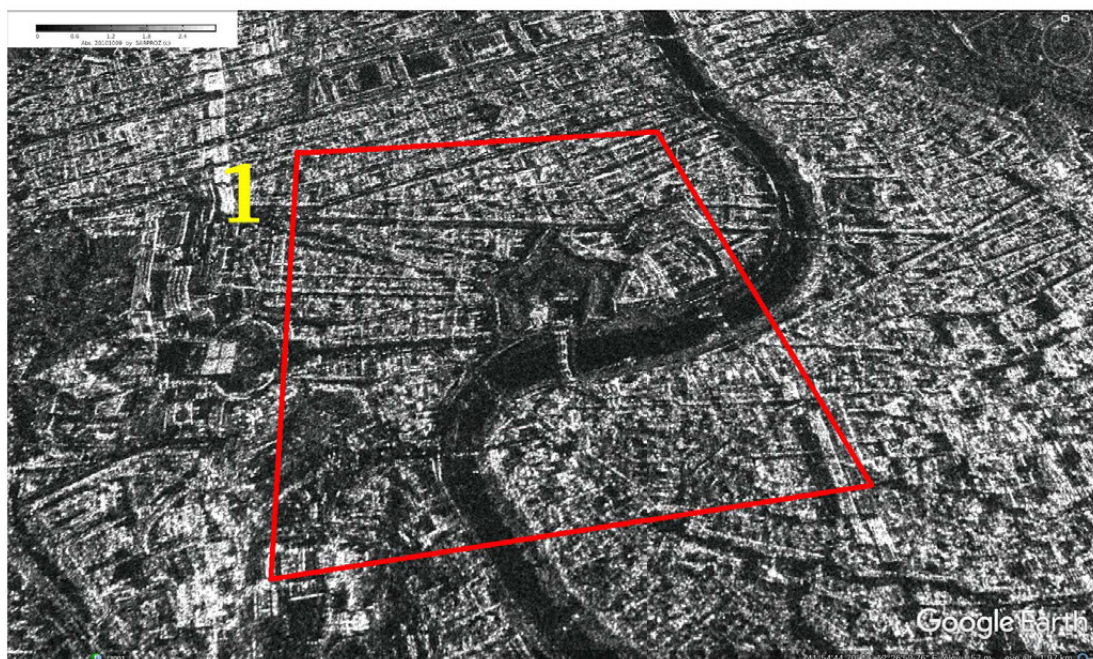


Fig. 6.34: River water-levels heights errors. (blue): measurement errors existing between the CSK observations versus ground-truths (no average). (red): Measurement errors existing between the CSK observations versus ground-truths (average window of 5 observations). (black): Measurement errors existing between the CSK observations versus ground-truths (average window of 10 observations).



(a)



(b)

Fig. 6.35: Geocoded SAR images.



(a)

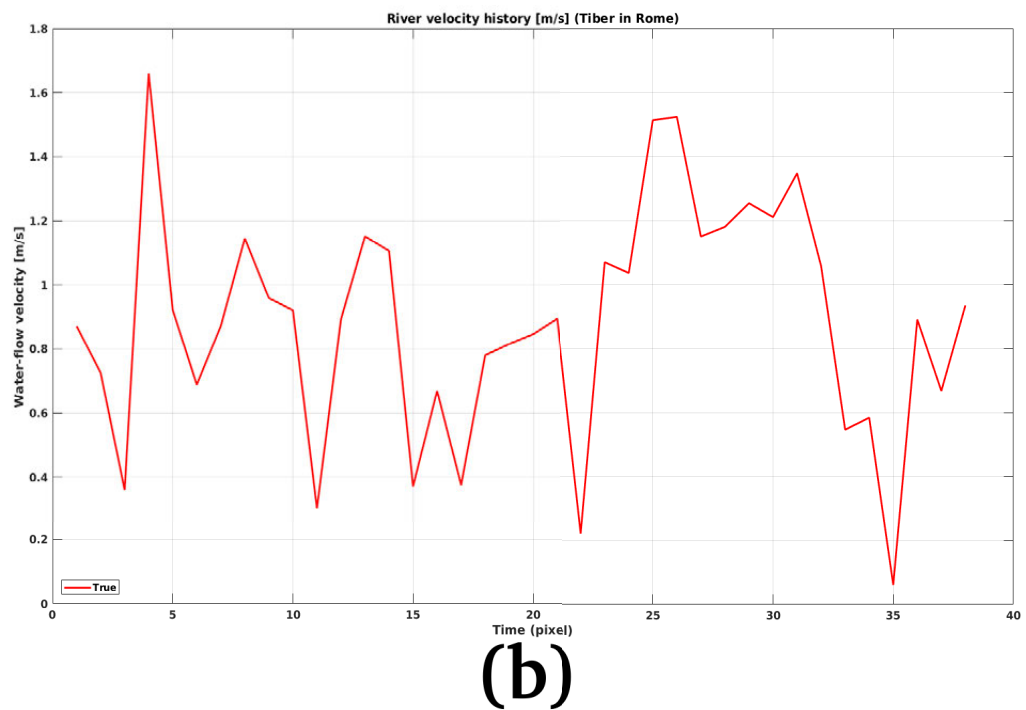


Fig. 6.36: (a): Marconi bridge located in Rome. (b): Estimated velocities.